The impact of CT image parameters and skull heterogeneity modeling on the accuracy of transcranial focused ultrasound simulations

Montanaro, Hazael; Pasquinelli, Cristina; Lee, Hyunjoo J.; Kim, Hyunggug; Siebner, Hartwig R.; Kuster, Niels; Thielscher, Axel; Neufeld, Esra

Published in:
Journal of Neural Engineering

Link to article, DOI:
10.1088/1741-2552/abf68d

Publication date:
2021

Document Version
Peer reviewed version

This document is the accepted manuscript version of the following article:
Montanaro, H., Pasquinelli, C., Lee, H. J., Kim, H., Siebner, H. R., Kuster, N., … Neufeld, E. (2021). The impact of CT image parameters and skull heterogeneity modeling on the accuracy of transcranial focused ultrasound simulations. Journal of Neural Engineering. https://doi.org/10.1088/1741-2552/abf68d

The impact of CT image parameters and skull heterogeneity modeling on the accuracy of transcranial focused ultrasound simulations

Hazael Montanaro[a,b,h,i], Cristina Pasquinelli[c,d,i], Hyunjoo J. Lee[e], Hyunggug Kim[e], Hartwig R. Siebner[c,f,g], Niels Kuster[a,b], Axel Thielscher[c,d], Esra Neufeld[a,b]

[a] *Foundation for Research on Information Technologies in Society (IT'IS), Zurich, Switzerland*
[b] *Department of Information Technology and Electrical Engineering, Swiss Federal Institute of Technology (ETH), Zurich, Switzerland*
[c] *Danish Research Centre for Magnetic Resonance, Centre for Functional and Diagnostic Imaging and Research, Copenhagen University Hospital Hvidovre, Denmark*
[d] *Center for Magnetic Resonance, Department of Health Technology, Technical University of Denmark, Kgs. Lyngby, Denmark*
[e] *School of Electrical Engineering, Korea Advanced Institute of Science and Technology, Daejeon, South Korea*
[f] *Department of Neurology, Copenhagen University Hospital Bispebjerg, Copenhagen, Denmark*
[g] *Institute of Clinical Medicine, Faculty of Health and Medical Sciences, University of Copenhagen, Copenhagen, Denmark*
[h] *Laboratory for Acoustics / Noise control, Empa, Swiss Federal Laboratories for Materials Science and Technology, Dubendorf, Switzerland*
[i] *The authors contributed equally to the work*

Abstract

Objective: Low-intensity transcranial ultrasound stimulation (TUS) is a promising non-invasive brain stimulation (NIBS) technique. TUS can reach deeper areas and target smaller regions in the brain than other NIBS techniques, but its application in humans is hampered by the lack of a straightforward and reliable procedure to predict the induced ultrasound exposure. Here, we examined how skull modeling affects computer simulations of TUS.

Approach: We characterized the ultrasonic beam after transmission through a sheep skull with a hydrophone and performed CT image-based simulations of the experimental setup. To study the skull model's impact, we varied: CT acquisition parameters (tube voltage, dose, filter sharpness), image interpolation, segmentation parameters, acoustic property maps (speed-of-sound, density, attenuation), and transducer-position mismatches. We compared the impact of modeling parameter changes on model predictions and on measurement agreement. Spatial-peak intensity and location, total power, and the Gamma metric (a measure for distribution differences) were used as quantitative criteria. Modeling-based sensitivity analysis was also performed for two human head models.

Main results: Sheep skull attenuation assignment and transducer positioning had the most important impact on spatial peak intensity (overestimation up to 300 %, respectively 30 %), followed by filter sharpness and tube voltage (up to 20 %), requiring calibration of the mapping functions. Positioning and skull-heterogeneity-structure strongly affected the

intensity distribution (Gamma tolerances exceeded in $>80\,\%$, respectively $>150\,\%$, of the focus-volume in water), necessitating image-based personalized modeling. Simulation results in human models consistently demonstrate a high sensitivity to the skull-heterogeneity model, attenuation tuning, and transducer shifts, the magnitude of which depends on the underlying skull structure complexity.

Significance: Our study reveals the importance of properly modeling the skull-heterogeneity and its structure and of accurately reproducing the transducer position. The results raise red flags when translating modeling approaches among clinical sites without proper standardization and / or recalibration of the imaging and modeling parameters.

Keywords:
transcranial focused ultrasound stimulation, skull modeling, treatment planning, image-based modeling, computational dosimetry, sensitivity analysis

1. Introduction

Low intensity transcranial focused ultrasound stimulation (TUS) has good spatial resolution and can also target deeper brain areas compared to established transcranial stimulation methods, offering a complementary application profile [1]. Its neuromodulatory effects have been repeatedly demonstrated in animals [2, 3, 4, 5, 6] and humans [7, 8, 9, 10], but its cornerstones still need to be better established in order to move TUS from basic research towards clinical applications. In particular, an accurate and precise control of the spatial distribution and intensity of the TUS beam is needed to ensure that neurally effective and safe stimulation doses are delivered in the brain.

While standardized procedures have been established to measure the profile of an ultrasound beam in water (for example IEC 62127-1 or [11]), the characterization of the beam profile in the brain after propagation through the dense, heterogeneous skull structure is a difficult problem for *in-vivo* applications in humans. The mismatch in acoustic impedance between the skull and the surrounding soft tissue and water strongly affects the TUS beam. In addition, the skull itself is composed of two outer layers of cortical bone with a layer of inhomogeneous cancellous bone inside, each having different density and thickness [12].

So far, computer simulations based on computed tomography (CT) images are considered the best choice for dose estimations for human TUS [13, 14, 15, 16, 17, 18, 19]. CT images offer a strong contrast between bone and other tissues, allowing for an accurate segmentation of the skull surfaces, and can further be used to estimate the bone density. Using the assumption that tissue density systematically relates to acoustic properties, several works [16, 17, 18] established mappings between the CT Hounsfield units (HU) and the acoustic properties of bone. This approach is promising, but still requires further development and validation, as the mapping of HU to density without further calibration typically only applies for soft tissue and not bone [20]. Small variations of the geometry and acoustic skull properties (speed-of-sound, attenuation) can significantly affect the dose shape, focus location and spatial peak intensity [21], suggesting the need for individualized dosing approaches.

To account for differences in scanner types and settings, CT attenuation grayscale values are typically mapped to the dimensionless linear scale of HU using air (-1000 HU) and water (0 HU) as reference points. The calibrated HU can then be mapped to the density of soft tissue, since most organs behave like water with regards to radiation physics [20]. This, however, does not hold strictly true for bone (between 300 and 3000 HU), as it further depends on the X-ray spectrum and beam hardening correction, which requires additional calibration [22]. Even after calibration, there is no linear map that correctly fixes the HU and density relation for air, water, and skull. Furthermore, clinical CT images lack the spatial resolution to fully resolve the microstructure of the highly heterogeneous cancellous bone layer.

Practically, this presents a challenge as the HU derived acoustic properties of bone now depend on scanner type and settings [23] (see Figure 1A for the impact of tube voltage on HU distribution in the sheep skull). The HU values outside the calibrated linear range of air and water depend on acquisition parameters such as the chosen tube potential, the current-time product, and the reconstruction filter (see Figure 2). In practice, CT parameters are set to minimize the radiation dose at the expense of image resolution and signal-to-noise ratio (SNR) for the application at hand. It is so far unclear how sensitive the simulated TUS beam profile is to variations of the dose and smoothness of clinical CT images, and how this affects the match between the simulated and real beam profile of TUS after transcranial transmission.

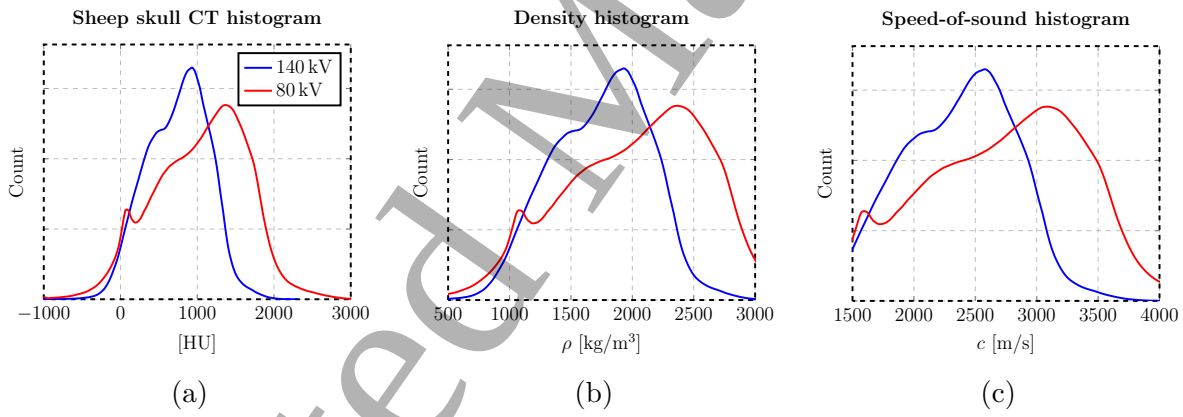

Figure 1: Histograms of HU values, skull density, and speed-of-sound (mapped linearly using air and water as anchor points) at two different CT tube voltages: 140 (blue line) and 80 (red line) kV. Clearly, the tube voltage affects the image-based property maps when no specific calibration is applied.

Compounding the issue are variations found between different mappings from bone density to acoustic properties (see Figure 3). The linear mapping from density to speed-of-sound from [16] has two free parameters that can be adjusted to compensate for the variations in the CT, while the non-linear mapping from [17] is fixed and derived for a particular CT configuration and stimulation frequency. The proper way to map image-derived density to skull acoustic attenuation map is still an open problem and its parameters are normally artificially tuned to match the experimental beam profile [21, 16, 24].

In this study, we investigated the impact of CT image parameters (energy levels, filter sharpness, and noise levels), of the skull shape reconstruction approach, of the different mappings from HU to acoustic properties, and of transducer positioning uncertainties on the simulated acoustic exposure from a single element focused transducer (SEFT) operated at 500 kHz.

Using a state-of-the-art clinical CT scanner, we acquired images of a sheep skull sample. The nominal image resolution was chosen as high as possible to allow for an accurate reconstruction of the object boundaries and the internal heterogeneous structure. The dose was varied to correspond to that of a standard clinical head scan (1–2 mSv), a low-dose scan previously used for research purposes (0.3 mSv) [25] and a high-dose one as comparison baseline. Image reconstruction was repeated with different filters that resulted in varying trade-offs between image smoothness and noise levels. While the majority of the images were acquired at a tube voltage of 140 kV, we also considered one image acquired with a tube voltage of 80 kV. The image HU were mapped to acoustic properties employing different transformations, such as the ones proposed by [16] and [17] (see Figure 3), and used to simulate acoustic transmission through a sheep skull, as further described in [19]. Systematic comparisons of the simulations with hydrophone measurements of the beam profiles allowed assessing the impact of the parameter choices on the accuracy of the simulations. The analysis distinguished between effects of the parameter variations on the focus shape and the magnitude, respectively, of the transcranial intensity distribution. As the pressure magnitude strongly depends on the attenuation in the skull that is often experimentally tuned for the particular model, skull attenuation was treated separately. To verify the transferability of the results to human skulls, a modeling-based analysis was also performed to investigate the impact of skull heterogeneity and attenuation modeling and the sensitivity to shifts of the transducer position.

The goal of this study is to provide guidance on the application of image-based skull modeling (imaging and image processing parameters, skull reconstruction, property mapping), to point out remaining limitations, and to give insight into the sensitive parameters dominating the modeling uncertainty.

2. Methods

2.1. Bone sample

In this study, we tested the same sample of sheep skull used in [19]. Soft tissue from the skull was mechanically removed with tweezers, and the sample was cut to maintain the upper section of the skull. The bone sample was then glued to a holder (see Figure 4) and subsequently continuously kept under phosphate-buffered saline (PBS) solution.

2.2. Measurements

A detailed description of how the ultrasound beam was characterized with hydrophone measurements of acoustic intensity in a water tank, with and without the skull, and how

we analyzed the data can be found in [19]. Briefly, we employed two function generators (33220A, Agilent Technologies, California, United States) to generate a burst (20 cycles / burst) of sinusoidal waves with a center frequency of 500 kHz, at a pulse repetition frequency of 1 kHz and a peak-to-peak driving voltage of 600 mV set at the function generator. The pulse was subsequently amplified by a power amplifier (5312, OPHIR, California, USA) and sent to a single element spherical ultrasound transducer (IPBD2, Hagisonic, South Korea, as in [19]). Two custom-designed 3D-printed holders were used to fix the transducer and the skull inside a tank at a specific distance between each other (see Figure 4). We measured the position of the transducer inside the holder using a caliper before each measurement series, and the position of the hydrophone-facing skull surface using a hydrophone phantom to calculate the distance between this surface and the transducer face. CT data (as described in Section 2.4.1) of the skull and the two holders were acquired, to be able to replicate the exact relative positioning of the transducer and the skull in the simulations. This distance was cross-checked with the measured distance. To sample the pressure wave, we employed a calibrated needle hydrophone (NH1000, Precision Acoustic, Dorset, UK) with an active diameter of 1 mm. The hydrophone was moved by a stepper-motor system (Sciencetown Co., Incheon, South Korea) with a plane sampling distance of 0.25 mm, and controlled by custom written software in Matlab. The voltage signal from the hydrophone was transmitted and visualized with an oscilloscope (DSOX2022A, Agilent Technologies, California, United States), transferred to a laptop and converted into pressure values using the hydrophone sensitivity in mV/MPa at 500 kHz (obtained from the manufacturer-provided calibration sheet). The intensity in W/m^2 was calculated from the pressure measurements as described in [19] according to $I = \frac{p^2}{2\rho c}$, where p is the pressure in Pa, ρ is the density of water (1000 kg/m^3), and c is the speed-of-sound in water (1500 m/s), while the deposited power density is obtained as $2\alpha I$.

The data analyzed in this paper was acquired with the sheep skull at a distance of 18.2 mm between the transducer and the surface of the skull facing the hydrophone (corresponding to 'position 1' in our companion paper [19]).

2.3. Simulation framework

Acoustic propagation was simulated with the same methodology as in [19] within the Sim4Life (ZMT Zurich MedTech AG, Zurich, Switzerland) platform employing the linear acoustic pressure wave solver (LAPWE) from [26]. The LAPWE solver solves the wave equation:

$$\rho \nabla \frac{1}{\rho} \nabla p - \frac{1}{c^2} \frac{\partial^2 p}{\partial t^2} - \frac{\tilde{a}}{c^2} \frac{\partial p}{\partial t} = 0 \tag{1}$$

where ρ is density in kg/m^3, c is speed-of-sound in m/s, p is pressure in Pa, t is time in s, ω is angular frequency in rad/s, and $\tilde{a}$:

$$\tilde{a} = 2\alpha \sqrt{\frac{\alpha^2 c^4}{\omega^2} + c^2}$$

where α is attenuation in Np/m. The acoustic properties assigned to the materials are listed in Table 1.

Voxel size in every material remained below a tenth of its wavelength with the coarsest grid step at 0.3 mm outside the skull region and 0.1 mm in the skull region, resulting in a simulation mesh with about 500 million voxels.

Simulations of the experimental setup were performed for a pure water background, as well as with the skull obstacle in a water background (see Figure 4B).

We carefully modeled the transducer in order to account for its internal structure and vibrational modes and to ensure accurate estimations of the beam transmission through complex obstacles [19]. The transducer model is identical to the P_1 model in [19], which distinguishes the outer, concave acoustic lens (matching layer made from acrylic resin, properties as in Table 1) and a disk shaped piezo-element (treated as Dirichlet pressure boundary condition with a sinusoidal 'aperture function' that accounts for the spatial variation of the pressure magnitude). The simulated exposure intensities are scaled such that the total deposited power in the measurement region matches the experimentally determined one for an obstacle-less water bath setup.

HU-based inhomogeneous property assignment was restricted to the skull region. Voxels were assigned to 30 different bone classes based on HU binning. An increase of the number of binning classes beyond 30 was found to not significantly affect the acoustic distributions anymore (less than 1 % change in spatial peak intensity).

2.4. Varied parameters

We defined a baseline configuration for the parameters used in acquiring the CT images and in setting up the simulations, and then varied them individually. Table 2 presents all parameter variations and the baseline parameters.

2.4.1. CT imaging of the skull

We acquired CT images of the skull attached to its holder in air background using a positron emission tomography / computed tomography (PET / CT) scanner (Biograph 128, Siemens, Germany). We acquired CT data with two tube potentials, 80 and 140 kV. The latter corresponds to the tube potential used in [17] for mapping HU to acoustic properties. Figure 1A shows the different distribution of HU for the two tube voltages. For 80 kV, a tube current-time product of 115 mAs was used, together with a sharp filter (H60s) during reconstruction. This corresponds to a low effective dose of ∼0.3 mSv for a human head scan (roughly one-third of the dose of clinical head scans) [25]. The spatial resolution was $0.36 \times 0.36 \times 0.6\,\mathrm{mm}^3$. For 140 kV, three current-time products were used: 300, 70, and 25 mAs corresponding, respectively, to a high (∼4.3 mS), clinical (∼1 mS), and low (∼0.3 mS) effective dose. The spatial resolution was $0.39 \times 0.39 \times 0.6\,\mathrm{mm}^3$. For each dose, three reconstruction filters were used, corresponding to three different filter levels (H60s: sharp filter, H48s: medium filter, H41s: smooth filter). As the image noise is not only dependent on the parameter settings, but also on properties of the scanned object such as size and density, Gaussian noise was added to the images acquired with H60s and H41s filters to emulate the noise levels of human images at low and clinical doses (see Appendix A for details). Table A.1 in the Appendix lists the adjusted noise levels of the images depending on the CT parameters. Table 2 gives an overview of the acquisition and reconstruction

parameters considered here. Figure 2 shows six examples of images acquired with different parameters.

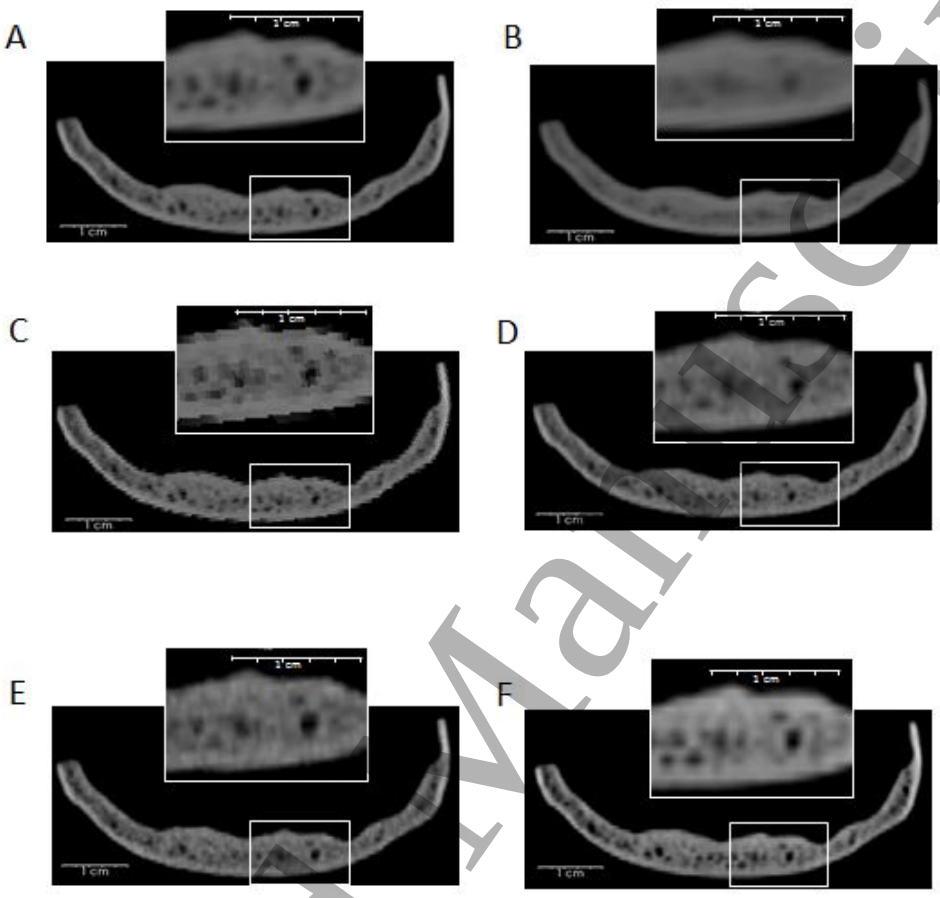

Figure 2: The figure shows six examples of the same slice of the sheep skull, acquired with different scan / processing parameters: (A) high-dose and sharp filter (H60s), (B) high-dose and smoother filter (H41s), (C) high-dose and sharp filter (H60s), with nearest-neighbor interpolation, (D) clinical-dose, sharp filter (H60s), (E) low-dose and sharp filter (H60s), and (F) with a tube voltage of 80 kV. When not indicated otherwise, the tube voltage was 140 kV, and linear interpolation was used. In images (D) and (E), additional noise was added to emulate typical human imaging conditions, as described in Appendix A. The insets show a zoomed region of the image, indicated by the white square. The images clearly show that the level of detail changes depending on the employed acquisition or reconstruction parameters.

2.4.2. 3D skull geometrical model

Skull model parameters were varied to assess their impact on the simulated beam. The skull models were generated by first thresholding the CT images at 0 HU (the skull CT images are acquired in air-medium where the background is around -1000 HU) to extract a surface model of the skull component. Image up-sampling via either nearest-neighbor or linear interpolation (baseline: linear) was applied to relate the coarse CT resolution to the fine discretization step in the simulation domain (0.112 mm).

	HU	$\rho\,[\mathrm{kg/m^3}]$	$c\,[\mathrm{m/s}]$	$\alpha\,[\mathrm{Np/m}]$
Air	-1000	1.275	343	0
Water	0	1000	1500	0
Sheep skull	*variable**	1710	2500	100
Matching layer	-	1190	2600	50

Table 1: Parameters used for skull property mappings, based on the approach from [16], but using species-specific values from [27]. *variable** indicates that the HU value of bone is scan parameter-dependent and defined here as the location of the corresponding HU-histogram peak.

Varied parameters	
CT imaging	
Tube voltage	80, ***140*** kV
Filter (smoothing)	H41s, H48s, ***H60s***
Dose	Low, Clinical, ***High***
Skull model generation	
Interpolation	Nearest neighbor, ***Linear***
Acoustic property mapping	
Speed-of-sound	Homogeneous, $\mathrm{Gaussian}_1$, $\mathrm{Gaussian}_2$, $\mathrm{Gaussian}_3$, $\boldsymbol{\mathrm{Linear}}_{w,s}$, $\mathrm{Linear}_{a,s}$, Pich_{836}, Pich_{500i}, Pich_{270}
Attenuation	0, 50, ***100***, 150, 300 Np/m, Pich_{836}, Pich_{500i}, Pich_{270}
Skull position	
Translation	***0***, ±1, 2, 3 mm
Rotation	***0***, ±1, 3°

Table 2: The different parameters considered in this paper and their baseline parameters (***italic+bold***; individual parameters are varied while keeping the other parameters at their baseline). The mappings are explained in detail in Table 3 and Section 2.4.3.

Image-based skull map parameters			
	HU $\rightarrow \rho$ ref_1, ref_2	$\rho \rightarrow c$ ref_1, ref_2	α [Np/m]
$\text{Linear}_{w,s}$	water, skull	water, skull	100
$\text{Linear}_{a,s}$	air, skull	air, skull	100
Pich_{836}	air, water	[17]	[17]
$\text{Pich}_{836,100}$	air, water	[17]	100
Pich_{500i}	air, water	interpolated [17]	interpolated [17]
$\text{Pich}_{500i,100}$	air, water	interpolated [17]	100
Pich_{270}	air, water	[17]	[17]

Table 3: The different acoustic property mapping schemes (density ρ, speed-of-sound c, and attenuation α). ρ is mapped from HU, and c from ρ. α is either mapped from density, or kept homogeneous. The mapping can be linear, with water and sheep skull ($\text{Linear}_{w,s}$), or air and sheep skull ($\text{Linear}_{a,s}$), as anchor points. In addition, the mapping can be non-linear, following the method proposed by [17]. In [17], mappings relative to two frequencies were studied (270 and 836 kHz, Pich_{270} and Pich_{836}). We also consider interpolated mapping functions to handle the 500 kHz (Pich_{500i}) frequency used in this study.

2.4.3. Skull acoustic property maps

Heterogeneity. The importance of considering skull heterogeneity and structure was investigated by either modeling the skull as a homogeneous medium or as heterogeneous with image-based tissue properties distributions (baseline, defined below). To test the impact of the structure of the skull heterogeneity on the acoustic beam, virtual images were constructed by replacing the skull's HU values with random values following a Gaussian distribution with the mean and standard deviation of the original HU value distribution (see Figure B.1) before the different acoustic property maps were applied. The spatial granularity of the assignment of the random values was varied (resolution: 0.1 mm, granularity: $1 \times 1 \times 1$ / $2 \times 2 \times 2$ / $3 \times 3 \times 3$ voxels). The mean wavelength inside the skull varies between 4.5–5 mm. The granularity was varied to range from the simulation discretization resolution to the imaging resolution.

Density and speed-of-sound. To simulate the inhomogeneity of the skull, we first used an approach similar to the one from [16] to map HU to acoustic properties. This approach was also explored in our previous study [19]. It assumes that the CT HU can be linearly mapped to bone density, which in turn maps to speed-of-sound according to the following relations:

$$\rho = \rho_{ref_1} + \frac{\rho_{ref_2} - \rho_{ref_1}}{HU_{ref_2} - HU_{ref_1}} HU$$

$$c = c_{ref_1} + \frac{c_{ref_2} - c_{ref_1}}{\rho_{ref_2} - \rho_{ref_1}} \rho$$

where ref_1 and ref_2 refer to the reference anchors (air, water or skull) of the linear mappings and their corresponding HU and density values. ref_1 is chosen as either water or air and

ref_2 as species specific average skull properties. As mentioned earlier, the HU of water and air are fixed by definition, however the average skull value is not. To set HU_{ref_2}, a histogram of the skull CT HU data was extracted and the HU value corresponding to the peak of the histogram was used. ρ_{ref_2} and c_{ref_2} were set to the species-specific average skull properties (density and speed-of-sound, respectively) as obtained from [27]. Adjusting the linear mapping to the peak HU of skull ensured that the density and speed-of-sound histograms of 80 and 140 kV acquisitions agreed reasonably (see Figure 5 vs. 1).

Additionally, the non-linear mappings from [17] were also explored (see Figure 3). These mappings have no free parameters since the linear HU to density conversion depends uniquely on water and air for calibration (which are independent of CT settings), and the mapping from density to speed-of-sound and attenuation are fixed and only depend on frequency. These mappings were established for a discrete set of frequencies (270 kHz and 836 kHz are the ones closest to the stimulation frequency of 500 kHz employed in this study). Therefore, simulations at 500 kHz were performed using the experimentally determined relationships at 270 kHz and 836 kHz, as well as a point-wise linear interpolation thereof.

Note, however, that these maps were obtained by fitting experimental data from human skulls. The density to speed-of-sound and attenuation curves do not necessarily translate to other species, as discussed in [19]. It is also important to note, that the curves have been fitted to provide good approximations in a certain range of densities. Outside that range, the extrapolated evaluation of these fitting functions is not suitable, and in this study, the mapped properties are treated as constant above 1200 and below 2600 kg/m^3 (corresponding to 200 and 1600 HU, respectively).

Parameters used for the different mappings are shown in Table 3. The mappings are reproduced in Figure 3 and the resulting distribution of acoustic properties inside the skull for the baseline CT settings are plotted in Figure 5.

Attenuation. Previous work has assigned skull attenuation α based on the bone density ρ, as in [16] and [17]. However, in [16], this relation is heuristically tuned to better match simulation results with measurements. This is justified as a way to account for microscopic back-scattering effects that cannot be effectively captured by even high resolution CT images [21, 16, 24]. [24, 28] instead suggest using homogeneous absorption maps in the skull, based on the finding that the introduction of heavy stochastic noise (greater than 20 %) into a previously homogeneous attenuation distribution has almost no effect on the transcranial field distribution [21].

To investigate the impact of attenuation, first homogeneous attenuation with varying attenuation coefficients (0 / 50 / 100 / 150 / 300 Np/m) were applied (baseline: 100 Np/m), and subsequently, the different image-based non-linear mappings from [17] at 270 and 836 kHz were used, as well as a linearly interpolated version at 500 kHz.

2.4.4. Positioning sensitivity

Sensitivity assessment was also conducted by running simulations with the skulls shifted (± 1 / 2 / 3 mm) and rotated (± 1 / 3°) along the principal axes. Positive rotations are defined in a counterclockwise direction around the stated plane with the origin at the skull's

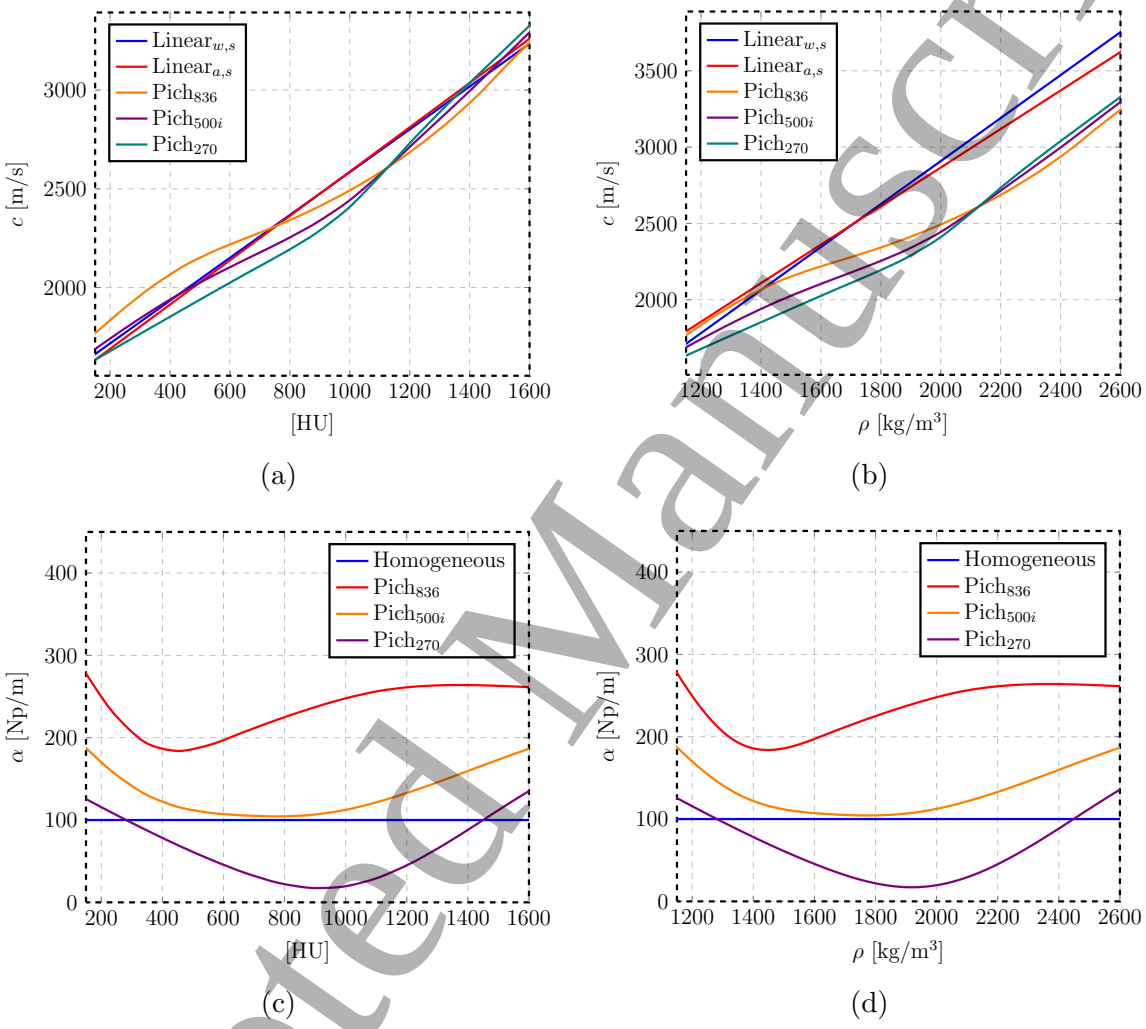

Figure 3: Speed-of-sound and attenuation mapping as a function of HU (A, B) and density (C, D). Up to 1700 HU, the combined ρ(HU) and $c(\rho)$ mapping results in mostly linear and equivalent c(HU) maps.

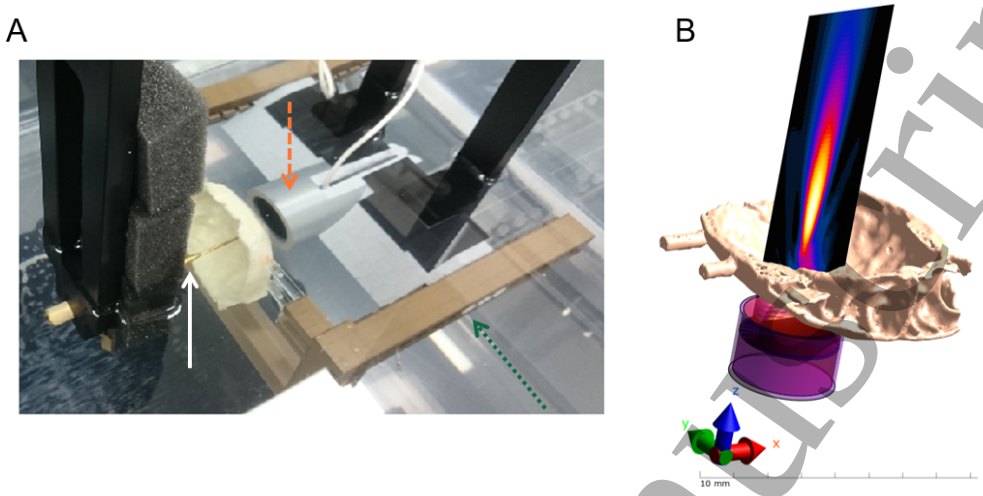

Figure 4: Setup used to characterize the ultrasound beam (A) and the corresponding simulation setup with results (B). In (A), three parts of the setup are visible: the hydrophone (white arrow), the sheep skull holder (green dotted arrow), and the transducer holder (orange dotted arrow). In the bottom corner of (B), the direction of the three Cartesian axes are indicated. Adapted from [19].

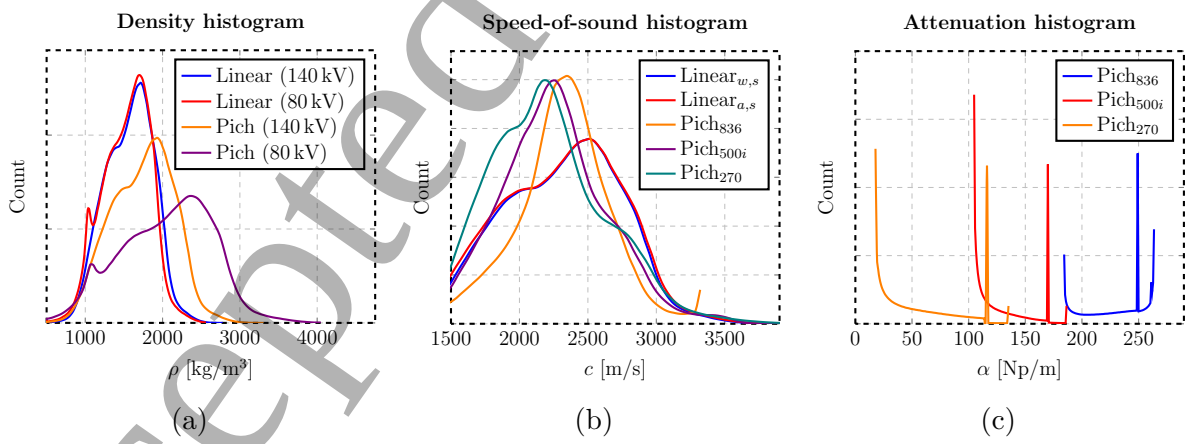

Figure 5: Density ρ (A), speed-of-sound c (B), and attenuation α (C) histograms for the different mappings.

bounding box center according to the right hand rule. The direction of the principal axes can be seen in Figure 4.

2.4.5. Human skulls

Simulations were performed using the *X10679* and *X62837* anatomical head models from [29], which established a collection of twenty detailed head models based on associated (co-registered) multi-modal image data that also encompasses CT scans. The models were selected as they were previously studied in [19]. For both head models, sonication of the left primary motor hand area ('Hand'; covered by thick, regular 3-layer sandwich skull) and the left primary motor leg area ('Leg'; underneath the sagittal suture) was simulated by positioning the transducer model from Section 2.3 such that its geometric focus coincided with the target location. While the original head models only distinguish cortical and cancellous bone (property assignment according to the values from [30]; referred to as 'homogeneous model'), skull heterogeneity was also modeled based on the CT scans using the $\text{Linear}_{w,s}$ and the Pich_{836} mappings. While the $\text{Linear}_{w,s}$ model used a constant attenuation of 27 Np/m (the value for cortical bone from [30]), the Pich_{836} mapping estimates both speed-of-sound and attenuation-heterogeneity from the CT data.

In addition, variants of the homogeneous and Pich_{836} models with the same constant attenuation as the $\text{Linear}_{w,s}$ model have been performed for the X62837 hand-target setup to enable separation of attenuation- and heterogeneity-related effects.

For all four setups, additional simulations have been performed for the $\text{Linear}_{w,s}$ models, in which the transducer has been shifted by 2 mm in two orthogonal directions perpendicular to the transducer orientation (referred to as x and y shifts).

2.5. Agreement metrics

We aimed to determine how sensitive the simulations are to changes of the parameters described above. To do so, we used one parameter combination as the reference case (highlighted in italic and bold in Table 2) and systematically varied single parameters to assess the impact on the simulated transcranial distribution. For quantitative analysis, we defined metrics to characterize both changes in the spatial beam profile (irrespective of the absolute intensity) and changes of the beam intensity.

In a second analysis, we tested how the parameters affected the fit between simulation and measurements, again using metrics that characterized the differences in beam shape and beam intensity, respectively. The employed metrics are described in detail below.

2.5.1. Comparison between simulations

We defined four measures to compare the spatial distribution and the intensity of the acoustic beam after skull transmission between simulations and the reference simulation:

Gamma comparison of the beam profiles: The Gamma method allows for a quantitative comparison of shape and intensity differences between two fields [31, 32, 19]. Here, we apply it to simulations that are first normalized to the total power in the volume after

the skull obstacle, resulting in a measure that is mostly sensitive to changes in the spatial beam shape, and not to the overall intensity.

The method relates differences between the distributions to acceptable spatial tolerances and an amplitude tolerance ($\Delta d_{x,y,z}$ and ΔD, respectively) defined by the user (see 2.5.3). It compares every point in the reference dataset with all points in the second dataset to determine the point in the second dataset that minimizes an Euclidean distance norm combining distance ($\vec{r}$) and value ($f(\vec{r})$) deviations, weighted by the corresponding tolerances:

$$\Gamma\left(\vec{r}_{\text{model}}, \vec{r}_{\text{ref},i}\right) = \sqrt{\frac{\left(f_{\text{model}}(\vec{r}_{\text{model}}) - f_{\text{ref}}(\vec{r}_{\text{ref},i})\right)^2}{\Delta D^2} + \sum_{j=x,y,z} \frac{\left(\{\vec{r}_{\text{model}}\}_j - \{\vec{r}_{\text{ref},i}\}_j\right)^2}{\Delta d_j^2}}$$

where i is the index of a specific point in the reference dataset, x, y and z are the spatial coordinate system of the two datasets, and the subscripts *ref* and *model* indicate the reference and the second dataset, respectively. A gamma index (γ) is subsequently assigned to each point by choosing the minimized Euclidean distance norm:

$$\gamma\left(\vec{r}_{\text{ref},i}\right) = \min\left\{\Gamma\left(\vec{r}_{\text{model}}, \vec{r}_{\text{ref},i}\right)\right\} \forall \vec{r}_{\text{model}}$$

In other words, it identifies the model point that best corresponds to it in terms of measured value and location, and determines the degree of agreement in terms of predefined tolerances. A value of $\gamma\left(\vec{r}_{\text{ref},i}\right) = 0$ corresponds to a perfect match for a point i, a value of $\gamma\left(\vec{r}_{\text{ref},i}\right) \leq 1$ means that the disagreement lies within the total tolerance, and $\gamma\left(\vec{r}_{\text{ref},i}\right) > 1$ means that the disagreement exceeds the combined tolerances. Finally, we determine the gamma comparison value $\gamma_{\%}$ for reporting, which is the volume in which gamma exceeds the threshold criterion, relative to the volume of the full width at half maximum (FWHM) of the beam in water background:

$$\gamma_{\%} = 100\,\frac{\text{volume with } \gamma > 1}{\text{volume of FWHM in water}} \tag{2}$$

This normalization allows comparison of the volume in which gamma exceeds the threshold to the overall volume of the beam. However, note that the gamma volume corresponds to positions both in- and outside the FWHM. See Figure 6 for an illustrative example of the Gamma comparison method.

Location of the spatial peak intensity $|d|$: We report the Euclidean distance $|d|$ in mm between the peak locations of the two distributions.

Spatial peak intensity: We report the difference between the peak intensities of the two simulations relative to the peak intensity of the reference case in percent:

$$\Delta I_{peak} = 100\,\frac{I_{peak,sim} - I_{peak,ref}}{I_{peak,ref}} = 100\,(\frac{I_{peak,sim}}{I_{peak,ref}} - 1)$$

where $I_{peak,sim}$ and $I_{peak,ref}$ are the peak intensity in the simulation and in the reference case, respectively.

Total power: Similarly to the peak intensity, we report the difference between the total power of the distribution after skull transmission, relative to the total power of the reference case:

$$\Delta P = 100\,(\frac{P_{sim}}{P_{ref}} - 1)$$

where P_{sim} and P_{ref} are the total transcranial power of the simulation and of the reference simulation, respectively.

2.5.2. Comparison of simulations to measurements

The above measures were adapted for the comparison of simulations and measurements as follows:

Gamma comparison of the beam profiles: Using the measurement data as reference, we changed the Gamma comparison by normalizing the intensity distributions of both simulations and measurements to their respective total power in a pure water background without obstacles. Total power calculations for the simulations and measurements were done over the same domain (the measurement volume in water). We refer to this Gamma metric as $\tilde{\gamma}_{\%}$.

Location of the spatial peak intensity $|\tilde{d}|$: We determined the Euclidean distance $|\tilde{d}|$ in mm between the peak locations in the simulation and measurement distributions.

Spatial peak intensity: We report the difference between the simulated and measured peak intensities, each normalized to the respective peak intensities in a pure water background, in % relative to the normalized peak intensity of the measurements:

$$\Delta\tilde{I}_{peak} = 100\,(\frac{I_{peak,sim}/I_{peakWater,sim}}{I_{peak,meas}/I_{peakWater,meas}} - 1)$$

where $I_{peakWater,sim}$ and $I_{peakWater,meas}$ are the peak intensities of the simulation and the measurements, respectively, in a pure water background without obstacles.

Total power: We report the difference between the simulated and measured total power of the distribution after skull transmission, each normalized to the respective total power in a pure water background ($P_{water,sim}$ and $P_{water,meas}$, respectively), in % relative to the normalized total power of the measurements:

$$\Delta\tilde{P} = 100\,(\frac{P_{sim}/P_{water,sim}}{P_{meas}/P_{water,meas}} - 1)$$

2.5.3. Tolerances for the Gamma comparisons

The chosen tolerances were motivated by the intended application – i.e., the spatially precise targeting of a small cortical patch – and the physical beam properties. Given a focus size of the used transducer with a FWHM in water with no obstacle of 42 mm along the beam axis and 5 mm perpendicular to it, we set $\Delta d_z = 5\,\text{mm}$ and $\Delta d_{xy} = 2\,\text{mm}$ as upper thresholds for shifts of the focus position in these directions. Shifts exceeding these criteria would result in the undesired stimulation of a neighboring cortical patch, or in a peak position that is in cerebral spinal fluid (CSF) or white matter, rather than in gray matter. A criterion of $\Delta D = 10\,\%$ was set as the amplitude tolerance, which is more conservative than the $\Delta D = 15\,\%$ used in our prior publication [19]. We updated it in order to make the Gamma comparison more sensitive to the impact of parameter changes on the power-normalized distributions, which can be expected to agree better with respect to amplitude.

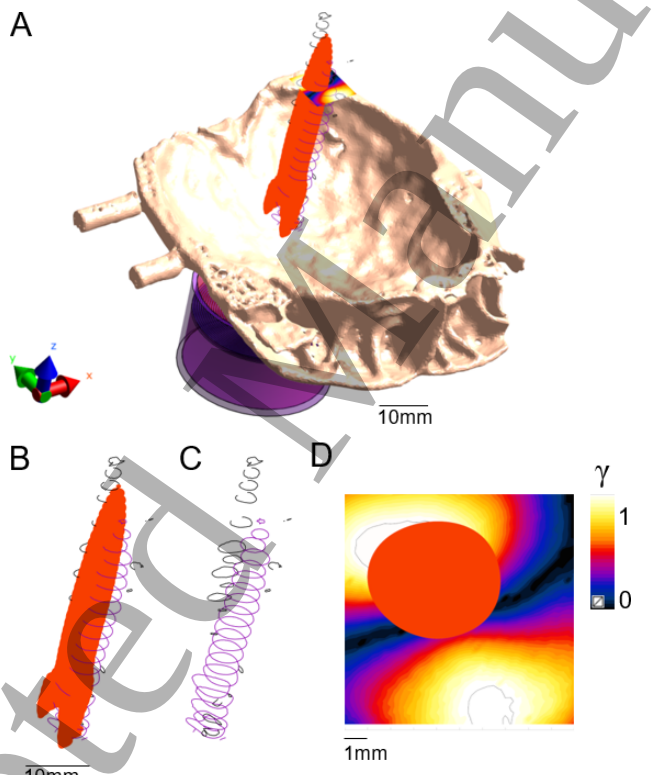

Figure 6: Simulated focus shape (intensity isolevel). The red iso-surface and violet iso-curves represent the 50 % level of the simulated and measured intensity distributions (after deposited power normalization). The black curves demark the regions where a γ-comparison value of 100 % is exceeded: (A) simulation setup, (B, C) enlarged focus region with and without simulation iso-surface display, and (D) view from the top displaying the full γ-distribution in a slice. (B) and (C) show that the simulated beam and measured beam point in slightly different directions and as such creates a corresponding mismatch of the gamma metric on one side of the beam (black curves).

2.5.4. Qualitative comparison

The impact of varying individual parameters on the simulated 3D intensity distributions were compared qualitatively through visualization of the maximum intensity projection (MIP) along the y-axis (see Figure 4B) onto a 2D plane containing the main axis of propagation (xz-plane). Figure B.2 shows sample MIPs with two different intensity normalization schemes: P_{sim} and P_{ref}, corresponding to the field scaling by the inverse of the simulation's total power or to the reference simulation's total power, respectively. Furthermore, the spatial distribution of $\gamma(\vec{r}_{\mathrm{ref}})$ provides an intuitive visualization of disagreement locations (see Figure 6 for an illustrative example of the Gamma comparison method).

3. Results

In the following, we refer to the Gamma metrics and peak location as measures of the spatial profile distribution (irrespective of the overall average absolute intensity), while we use the peak intensity and total power as measures of the magnitude of the distribution.

3.1. Impact of CT Parameters

Figure 7 summarizes the sensitivity of the simulations to changes of the imaging parameters (red curves) and the dependence of the fit between simulation and measurements on these parameters (blue curves). Overall, the simulations are only moderately sensitive to the tested imaging parameters, with the strongest impact seen for the peak intensity and total power, that vary up to 20 % between the two tube voltages and the different filter settings. However, it is worth noting that we fixed the peak of the bone density histogram to the value taken from literature (see Figure 5A). The choice of the interpolation scheme for upsampling (nearest-neighbor vs. linear) had only a small impact on the simulation results, likely due to the inherent smoothness of the underlying images from a clinical CT scanner.

None of the tested parameter variations strongly influenced the fit between simulated and measured spatial distributions (difference in Gamma up to 20 % and in Euclidean distance up to 0.15 mm), indicating that error sources such as measurement errors and coregistration errors between simulations and measurements likely contributed to the mismatch (see Section 3.3.1 below for details). These error sources might in part also explain the underestimation of the peak intensity and total power by the simulations that was observed in most cases. This is more apparent for the total power that was underestimated in the order of 20–30 %. The different behavior for peak intensity and total power indicates that while the simulations underestimate the deposited power, they simultaneously tend to overestimate the focusing quality, thus partially compensating the intensity underestimation in the beam center.

Additional visualizations of the beam distribution can be found in Figures B.2 and B.3 in the Appendix. Visual inspection of the MIP of the simulated acoustic intensity maps confirm the overall weak impact of the parameters on the simulated beam. Particularly, we observed a good match in the main lobe, while the strongest changes occurred in the transducer near-field, i.e., closer to the skull (see Figure B.2).

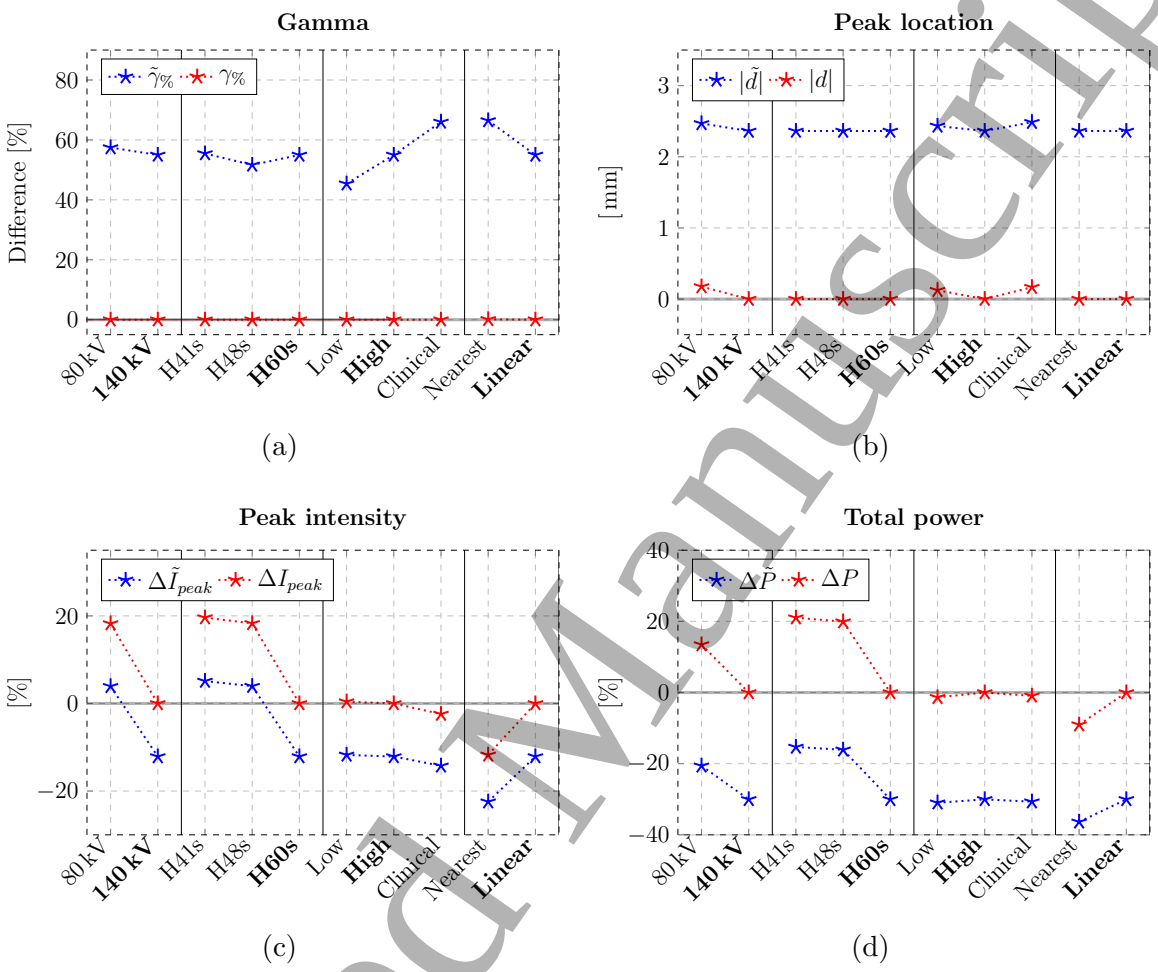

Figure 7: Dependence of (A) the Gamma metrics ($\gamma_{\%}$ and $\tilde{\gamma}_{\%}$), (B) the Euclidean distance between the location of the spatial peak ($|d|$ and $|\tilde{d}|$), (C) the peak intensity (ΔI_{peak} and $\Delta\tilde{I}_{peak}$), and (D) the total power (ΔP and $\Delta\tilde{P}$) on: Tube voltage, reconstruction filter settings, dose, and interpolation scheme during upsampling. The red lines show the comparison with the chosen reference simulation case (the reference parameters are highlighted as bold labels on the x-axis). The blue lines show the comparison to the acoustic measurements. The horizontal gray line at $y = 0$ corresponds to a perfect match with the reference for the particular metric. For example, all the red points in the Gamma comparison lie on the gray line, since they are all zeros, which means that for all measurement points there is a corresponding simulation point with a combined tolerance-normalized location- and value-deviation below 1. See Section 2.5 for a detailed description of the metrics.

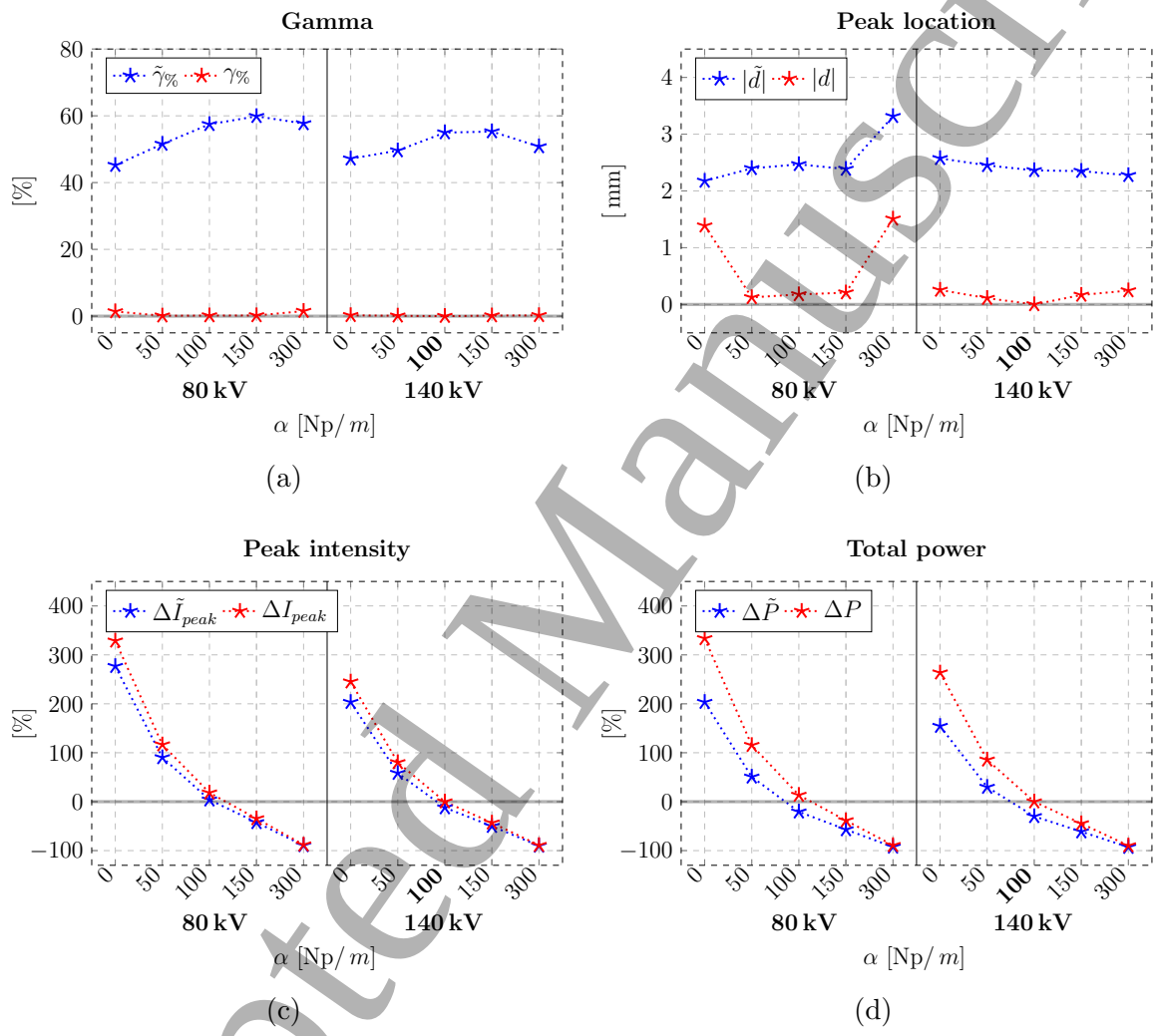

Figure 8: Dependence of the simulations on tube voltage and skull attenuation. Metrics as in Figure 7.

3.2. Impact of skull properties and mappings from CT to acoustic properties

3.2.1. Attenuation

The spatial distribution of the simulated beam is slightly affected by the attenuation of skull (red curves in Figure 8A and B), with a change in peak position up to 1.5 mm.

Correspondingly, the fit between simulated and measured beam profiles did not strongly change with the simulated skull attenuation (see blue curves in Figure 8A and B), with a maximum attenuation-related change of the Gamma metric of 20 % and less than 1.5 mm in peak position. Visual inspection revealed that the beam profile after skull transmission became increasingly smooth with increasing attenuation (right column of Figure B.4), without a strong change in its distribution.

In contrast, the skull attenuation had a profound impact on the intensity magnitude, with a mismatch of up to 300 %, of the simulated beam (see Figure 8C and D), as expected. A good fit between simulations and measurements was obtained for an attenuation of $\alpha = 100\,\mathrm{Np/m}$. However, this value is known to be species-dependent [14, 33, 34, 35] and subject to a large uncertainty. It is thus unclear whether the good fit in intensity observed here would translate to human applications.

3.2.2. Heterogeneity

Structure. Motivated by the weak impact of the skull attenuation on the spatial beam profile, we wanted to additionally test the relevance of accurately modeling the heterogeneous spatial distribution of the skull density and speed-of-sound in the simulations. Therefore, we modeled the skull as a homogeneous medium (using the values for the sheep skull in Table 1) and as random heterogeneous region (Gaussian distribution with mean and standard deviation matching that of the HU values in the skull, see Figure B.1 for details). We compared the results to those of our reference case with a linear mapping of the acoustic properties from the CT HU values ($\mathrm{Linear}_{w,s}$). Neglecting the internal structure of the skull and replacing it by a homogeneous region or Gaussian noise strongly affects both the spatial distribution and intensity of the simulated beam, with a mismatch up to 120 % in peak intensity and 100 % in Gamma (see red curves in the left part of the four sub-figures in Figure 9). Also, the fit to the measurement beam is generally decreased compared to the reference case, with a mismatch up to almost 100 % in peak intensity and almost 150 % in Gamma (see Figure 9 left part of the four sub-figures, blue curves).

Sample cross sections of the speed-of-sound distribution inside the skull with the corresponding beam profiles can be seen in Figure B.5. Visualizations of the FWHM envelope of the beam together with the γ-distribution show that homogeneous or random-Gaussian material properties result in more focused, symmetrical and smoother intensity distributions (see Figure B.6). This is in disagreement with the measurement results and increases the γ-errors on the two sides of the main lobe.

HU to properties mapping. After confirming the importance of modeling the heterogeneity of the skull, we compared the impact of different linear and non-linear mapping schemes that relate the HU values in the CT to the acoustic properties of bone. The linear maps are only used to generate the distributions of bone density and speed-of-sound, while attenuation

is modeled as spatially homogeneous in the skull. We used either water and cortical bone (reference case) or air and cortical bone as reference anchor points to establish the linear mappings. The tested non-linear mappings are based on the approach presented in [17], which includes mapping functions from CT density to speed-of-sound and attenuation at 270 kHz and 836 kHz. We linearly interpolated these two maps to also construct a mapping function for 500 kHz (Table 3 provides a summary of the tested mappings). We aimed to separate the effect of the mapping of the speed-of-sound and density from the effect of the mapping of the attenuation. Therefore, we also considered two skull models with the non-linear mappings for speed-of-sound and density from [17], but with a constant attenuation of 100 Np/m ($\text{Pich}_{836,100}$, $\text{Pich}_{500i,100}$). This attenuation was chosen as it gave overall the best match with the measurements (as highlighted in Section 3.2.1).

The results for the two linear mappings are nearly identical, independent of the selection of the lower anchor point (see right halves in Figure 9). Importantly, however, changing the value of the upper anchor point (here set to the peak of cortical bone) can be expected to have a large impact on the simulations.

The non-linear mappings (Pich_{836}, Pich_{500i}, Pich_{270}) that also estimate the position-dependent attenuation from the CT affect the fit between the simulated and measured spatial beam profiles only moderately, with a mismatch in peak position of up to 3 mm, and the mappings for 270 kHz even improve the Gamma metrics by 25 % (blue curves, Fig. 9A and B). However, the beam intensity varies strongly between the non-linear mappings (right halves, Figure 9C and D), with a mismatch up to more than 100 %.

When non-linear speed-of-sound maps with homogeneous attenuation were employed ($\text{Pich}_{836,100}$, $\text{Pich}_{500i,100}$), the shape of the normalized pressure distribution were rather similar to those obtained using heterogeneous attenuation maps (Pich_{836}, Pich_{500i}, see Figure 9A and B). However, the intensity prediction improved when the attenuation was kept constant (see Figure 9C and D), with a mismatch in power and peak intensity close to 0 %. These results indicate that attenuation mainly affects the overall intensity of the acoustic beam after skull transmission, while the the speed-of-sound and the density mainly affect the spatial distribution.

3.3. Positioning

The skull was shifted along and rotated around the main axes in the simulations. In general, shifts and rotations have a large, non-linear impact on focus location and intensity. This is due to the variation of skull thickness, skull heterogeneity and the changing orientation of the skull surface relative to the propagation axis. The data are shown in Figures 10 and 11.

3.3.1. Translation

The simulations are sensitive to small translations (red curves in Figure 10). In particular, shifts in the y-direction by 1 mm already result in changes of the peak intensity by more than 50 % and a shift of the peak position by 3 mm. The high sensitivity to shifts in this particular direction is likely caused by the associated changes in the distance between the skull interface and the transducer in combination with changes in the incidence angle of

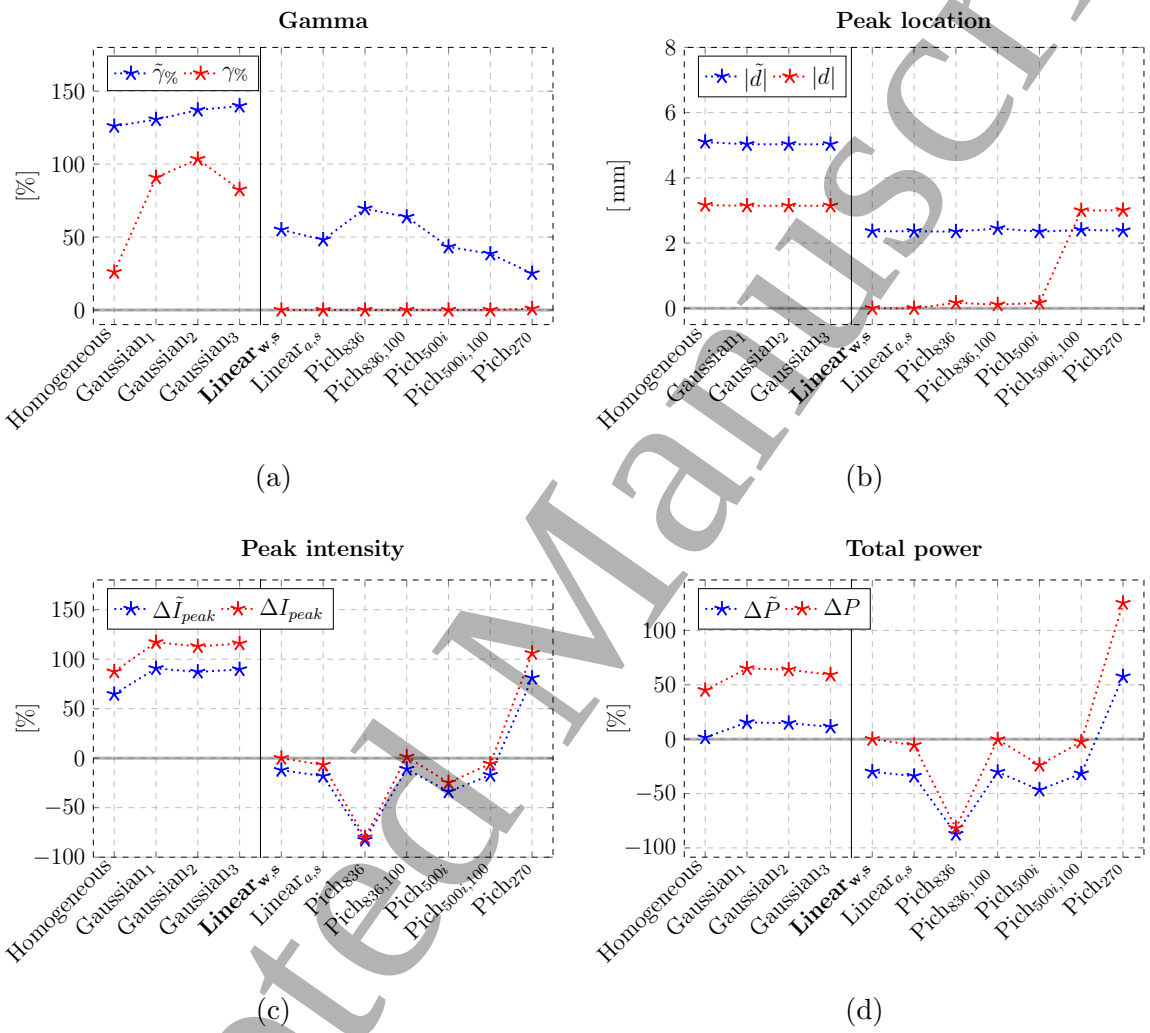

Figure 9: Dependence of the simulations on the modeling of the acoustic properties of the skull. Metrics as in Figure 7. See Table 3 for further details.

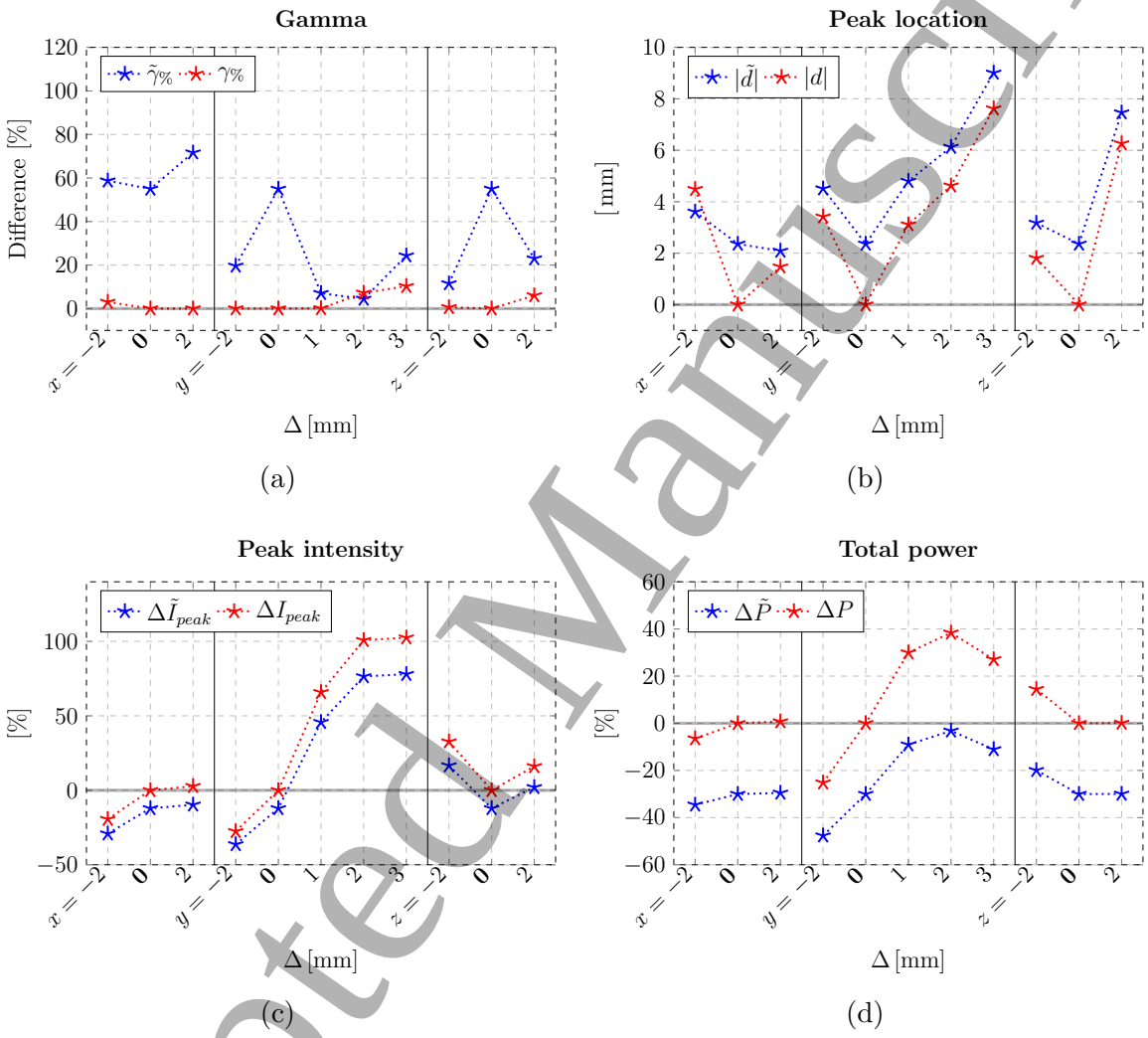

Figure 10: Dependence of the simulations on translations of the skull. Metrics as in Figure 7.

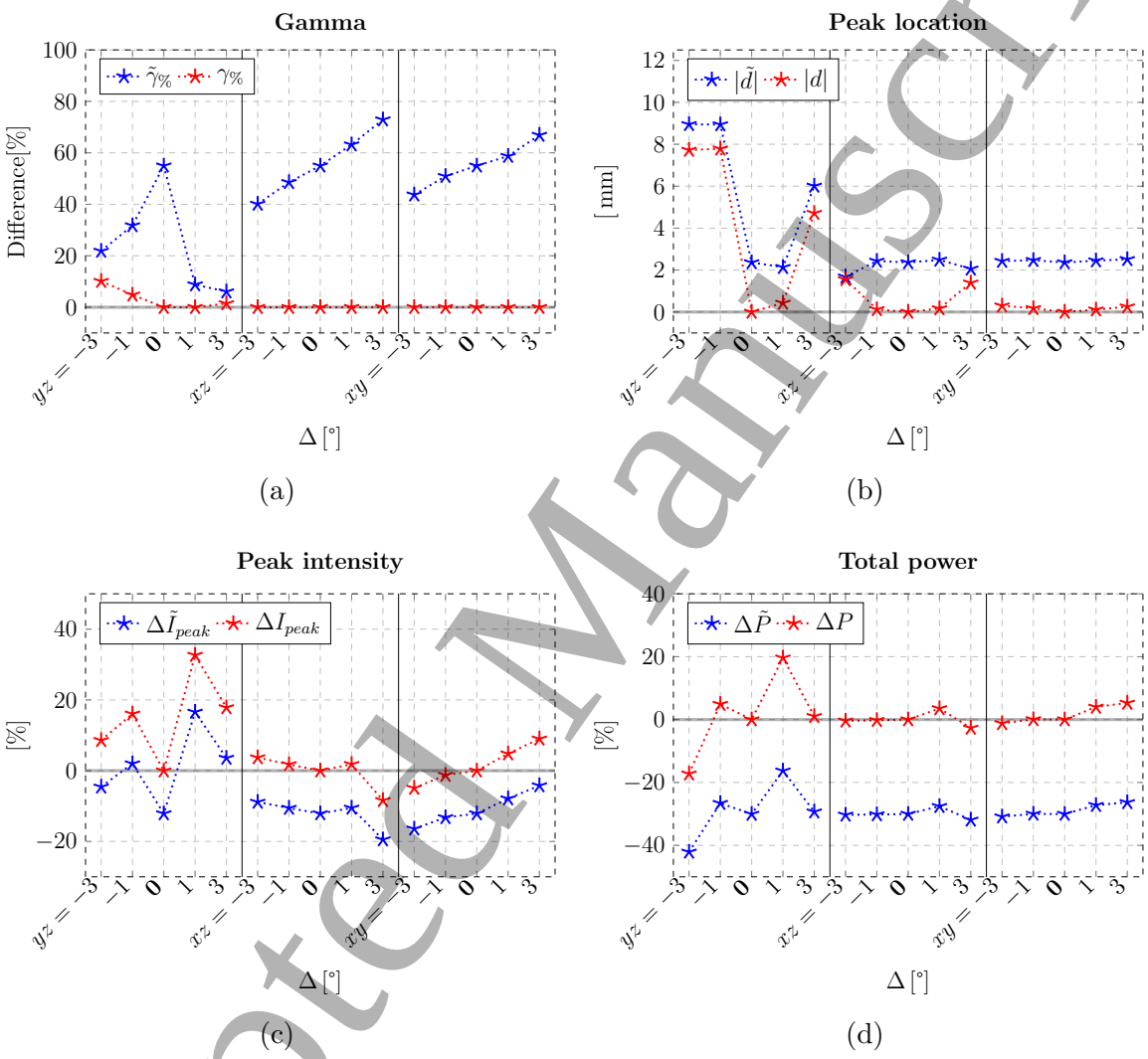

Figure 11: Dependence of the simulations on rotations of the skull. Metrics as in Figure 7.

the beam due to changes of the orientation of the skull surface in the beam center (see Figure 4). Due to the irregular shape of the skull, this effect is more pronounced for shifts in the y-direction (the anterior - posterior direction; deviations up to 100 % in peak intensity and 8 mm in peak position), than in the x-direction (medial - lateral direction; deviations up to -40 % in peak intensity and 4 mm in peak position). The Gamma metric is on average slightly affected by shifts, with a maximum variation of 10 %.

Comparison to the measurements (blue curves in Figure 10) in general confirm the importance of an accurate control of the transducer position relative to the skull, but does not allow for a straightforward identification of the cause of the differences between simulations and measurements. Specifically, while the peak position and peak intensity seem to be best matched for the reference case without shifts (3 vs. up to 9 mm for peak position and -10 % vs. up to 80 % for peak intensity), Gamma and total power are better matched for shifts in the positive y-direction, with an improvement of 50 % and 30 %, respectively. Correspondingly, visualizations of the FWHM envelope of the beam together with the γ-distribution indicates that the γ distribution of the reference case has high values (frequently exceeding 1) on two sides of the main lobe that are reduced for shifts in the positive y-direction (see Figure B.7A vs. B). This suggests a systematic slight shift of the lobe relative to the measurements, which can result from a simulation-related focus shift, or of inaccuracy in reproducing the exact skull or sensor position relative to the transducer.

3.3.2. Rotation

In general, the simulations are less affected by rotations in the tested range than they are by the translations (see red curves in Figure 11). Rotations in the yz-plane (i.e., rotations around an x-axis centered in the skull), however, have a strong impact, with a mismatch up to 10 % in Gamma, 8 mm in peak location, 35 % in peak intensity and 20 % in power, which is in line with the observed impact of translations along the y-direction. We suggest that the same structural features of the skull as described above for shifts in the y-direction also cause the sensitivity of the simulations to the rotations in the yz-plane.

The fit to the measurements is most sensitive to rotations in the yz-plane, and counterclockwise rotations improve the fit, with an improvement of 50 % in Gamma and 10 % in power (see Figure B.7A vs. C). Conversely, rotations around the xz-plane gradually sharpens the focus and shifts it further away, resulting in worse agreement (see Figure B.7D). As in the case of the tested translations, there is no particular rotation that results in the best fit in all measures, making the identification of the root cause of the differences difficult.

3.3.3. Human skulls

The results from the modeling-based sensitivity analysis of the setups involving human head models can be found in Table B.2 and Figures B.8 and B.9. They are in line with the experimentally validated simulation results for the sheep skull. When using the original mappings without adapting the attenuation, the peak intensity can vary by more than a factor of 50 compared to the reference configuration ($\text{Linear}_{w,s}$), with the biggest deviations seen for the Pich_{836} model (not surprising, considering that the CT images for the head models were acquired with scanner settings that likely differed from the ones used by [17]). In

most cases, the sensitivity of the focus location to changes of the skull heterogeneity modeling and shifts of the transducer remained below our tolerance threshold (see Section 2.5.3). Looking at the Gamma metric as a similarity measure of the (power normalized) intensity distribution, it is evident that the two heterogeneous models produce more similar results than the homogeneous model (deviations exceeding the tolerance are mostly restricted to volumes smaller than the FWHM volume in water between the heterogeneous models, while they can reach over 30 times that volume for the homogeneous models). The Gamma metric also shows that 2 mm shifts always produce unreliable predictions. When comparing the average Gamma values of the Hand targets to those of the Leg targets, it is evident that the sensitivity of the modeling results is smaller for the Hand targets in all cases (most apparent for the homogeneous modeling – 0 % vs. 185 %; about a factor of two for each of the x and y shifts). This can be explained by the simpler structure of the obstructing skull segment (mostly planar arrangement of cortical and cancellous skull layers vs. suture). Analyzing the power-normalized peak intensity (a focality metric), it is apparent that the sensitivity to 2 mm shifts is larger than the impact of heterogeneity modeling (the latter is smaller than the 10 % tolerance threshold in half of the setups). Separating the contributions of modeling the heterogeneities of speed-of-sound versus attenuation (only performed for the X62837 Hand setup) reveals that modeling the heterogeneity of skull attenuation hardly matters after power normalization and the modeling results are primarily sensitive to changes of the modeling of the speed-of-sound heterogeneity.

4. Discussion

General relevance of modeling the internal structure of the skull. Our results confirm the importance of accounting for the internal structure of the skull in order to accurately estimate the transmitted acoustic wave [36]. Simulations employing a homogeneous skull model, similar to those used in some prior studies [8], resulted in sharper foci and more regular and symmetric lobe shapes than observed in our measured distributions and in the simulations using CT-based acoustic skull properties (see Figure B.6). A similar disagreement with the measurements was also seen for simulations based on unstructured, random skull heterogeneities. Presumably, CT-based skull modeling introduces a structured heterogeneity that more profoundly distorts the wave front than homogeneous and random-heterogeneous skull properties. The latter mainly affect the skull transmission through reflections at the skull boundaries that might also cause standing-wave effects [19]. Modeling CT-based structured skull heterogeneity also tends to predict a reduced focus intensity – likely due to scattering and dephasing –, but also predicts suppressed side-foci (also a consequence of dephasing), which would be beneficial effect from a clinical perspective. While it seems generally useful to consider image-based information about skull structure in the simulations, the results can depend strongly on various imaging and image-processing choices made by the user. As detailed in the following paragraphs, this includes the CT imaging parameters, the strategies used to facilitate transferability between CT scanners or scanning protocols, and the mapping functions from CT HU values to acoustic properties.

Impact of CT parameters. Varying the imaging parameters and interpolation schemes had small to moderate effects on the simulations and their accuracy. In particular, the result indicate that the chosen CT dose (and by that the noise levels) did hardly affect the simulations that were based on a linear mapping between CT HU values and bone density. This is particularly important for future applications in humans, where it is preferable to minimize the X-ray dose. On the other hand, changing the filter sharpness and tube voltage moderately changed the simulations, in particular the estimated peak intensity and total power. Thus, controlling for these parameters and clearly documenting them in publications seems useful to improve the comparability of simulation results between studies. In this respect, it is important to note that the obtained HU values of the skull sample were clearly affected by the tube voltage. This is not unexpected, as the HU values of CT scanners are usually only calibrated and linear within the range corresponding to air (-1000 HU) and water (0 HU). Achieving a good correspondence between the simulation results obtained for the two tube voltages thus required us to rescale the HU values by choosing upper anchor points for the linear mappings that corresponded to the peak of the HU histograms (representing compact bone). While this was effective in reducing the dependence of the simulation results on the CT tube voltage, this approach would in practical applications also remove interindividual differences in bone density and speed-of-sound values.

Predicting the spatial distribution of the transmitted acoustic wave. Surprisingly, the tested linear and non-linear mappings from HU to acoustic skull properties resulted in similar predictions of the spatial distribution of the transmitted acoustic wave. This was on first sight unexpected, as the modeled range of bone densities differed clearly between the linear and non-linear mappings (see Figure 5A), with the non-linear mappings predicting on average higher densities. However, the mappings from density to speed-of-sound also differed between linear and non-linear mappings (see Figure 3C). These two differences partly compensated for each other, so that the resulting mappings from HU to speed-of-sound (see Figure 3A) were again mostly similar.

However, the spatial distribution of the transmitted wave is also affected by the amount of scattering inside the skull that is estimated by the linear and non-linear mappings. Spatial variations in bone density cause variations in acoustic impedance ($Z = \rho c$) and hence scattering. The term $\rho\nabla(\frac{1}{\rho}\nabla p)$ from Equation 1 can be rewritten as $\Delta p + (\rho\nabla\frac{1}{\rho})\cdot\nabla p$, so the contribution of density heterogeneity results from the $(\rho\nabla\frac{1}{\rho})$ term. The speed-of-sound histograms (see Figure 5B) show that the non-linear mappings result in narrower distributions than the linear ones and thus generally in reduced scattering predictions. Finally, comparing the histograms of the three non-linear mappings with each other reveals a right shift and narrowing of the distribution for 836 kHz compared to 270 kHz, which increases the focality of the predicted acoustic beam.

Obviously, attenuation strongly and predominantly affects the magnitude of the acoustic intensity distribution (see below). However, comparing the image-based speed-of-sound mapping used with homogeneous attenuation vs. CT-based heterogeneous attenuation maps indicates an improvement in focus location prediction when considering attenuation heterogeneity – a finding that differs from [21], because only stochastic heterogeneity was consid-

ered in that study.

Predicting the magnitude of the transmitted acoustic wave. While we found that using CT-based acoustic property maps helped to better estimate the spatial distribution of the acoustic wave after skull transmission compared to a homogenous skull model, a more complex pattern arose for the estimation of the magnitude of the transmitted wave. The latter is mostly affected by the acoustic attenuation of the skull. As noted by [16, 24], even high resolution CT is not detailed enough to account for acoustic attenuation related microscopic backstattering effects. Therefore an empirical relationship is employed. Some groups [28, 21] have advocated for a constant skull attenuation. For the linear mappings, we selected a spatially homogeneous attenuation value that resulted in a good match between the simulated and measured intensity. The optimized value of 100 Np/m fell within the range of attenuation values reported in literature ([17] reports 34 Np/m at 270 kHz and 200 Np/m at 836 kHz, see as well [27, 13, 30]), confirming that this is a meaningful choice. The resulting peak intensity and the total power was on average still underestimated by up to 40 %, and could likely have been improved further by fine-tuning the chosen attenuation (see Figure 7). However, this approach is not feasible for simulations of the TUS beam in human in-vivo applications. Rather, we then have to rely solely on attenuation values reported in the literature. Unfortunately, values between $\alpha = 10$ and $\alpha = 300$ Np/m have been reported for humans [17, 37], making the simulated intensities uncertain (see Figures 8C and D). In addition, attenuation might exhibit interindividual variations that are lost when assigning a constant value from literature.

The non-linear mappings suggested in [17] aimed to resolve these problems by also estimating a position-dependent attenuation value from the CT image. In addition, they do not involve a rescaling of the CT HU values, as we had to use for the tested linear maps. Thus, the proposed non-linear mappings provide comprehensive informing about the spatial distributions of bone density, speed-of-sound and attenuation inside the skull, including interindividual differences of the acoustic properties. In its current form, however, this approach unfortunately still suffers from two major limitations. First, as already discussed above, CT images are usually not calibrated in the higher HU ranges. Thus, a mapping from HU values to bone density that was established for a particular CT scanner cannot be unambiguously applied to data acquired from another scanner. Even for the same scanner, changing the image resolution or the reconstruction kernel affects the mapping [23], as it influences the spatial resolution at which density variations are resolved and thus affects scattering predictions. In addition, these parameters determine how severely partial volume effects at transitions between different materials such as compact and spongy bone will affect the non-linearly mapped tissue properties. The mappings must also be adapted when changing the tube voltage (see Figure 1). Here, we aimed to ameliorate the latter problem by using the same tube voltage as in [17] (140 kV, personal communication by the authors). It is still likely that the data from the CT scanners used here and in [17] differed in the upper HU range.

Second, the mappings were established for specific ultrasound frequencies, and need to be adapted when applied at other frequencies. In our results, this becomes apparent

when using the original mappings for 270 kHz and 836 kHz to estimate the acoustic wave at 500 kHz. The simulated peak intensity and total power strongly deviates by around 100 % for Pich_{270} and by -90 % for Pich_{836} (see Figures 9C and D), which corresponds to the results for constant attenuation values of the skull of about 50 and 300 Np/m, respectively, when using a linear mapping (see Figures 8C and D). This can be understood when analyzing the mapping functions. Attenuation as a function of HU are non-monotonous relationships for the Pichardo models (see Figure 3C). The 270 kHz transfer function oscillates around the constant attenuation value used for the homogeneous model, being lower in the 300–1400 HU range and higher elsewhere. Applied to our CT data, the resulting histogram of the attenuation values inside the skull (see Figure 5C) has two peaks – one around 20 Np/m (reflecting the shallow minimum of the transfer function at medium HU) and one around 115 Np/m (reflecting the flat transfer function at high HU) – and is on average clearly lower than the constant attenuation value of $\alpha = 100$ Np/m used for the linear mappings. The 836 kHz transfer function is much higher than the constant attenuation value used for the homogeneous modeling throughout the spectrum. Correspondingly, also the histogram of the attenuation values ranges from 180 Np/m to 270 Np/m (see Figure 5C).

While it was expected that the non-linear mappings that were established at too low (270 kHz) and high (836 kHz) frequencies resulted in under- and overestimated attenuation values, our results indicate that estimating a transfer function at an intermediate frequency through interpolation improves the results. However, as the shape of the transfer functions strongly and non-linearly depends on the frequency and the transfer functions are only available for a sparse set of frequencies, interpolation to other frequencies, e.g. at 500 kHz in our case, should be performed with caution and awareness. The comparison of Pichardo mappings used with homogeneous vs. image-based attenuation demonstrates that deviations from the measurements are influenced (and probably caused) by both speed-of-sound and attenuation heterogeneity.

The Pichardo [17] models were established for human skulls, so that a part of the mismatch between simulated and measured intensities might also stem from species- and age-specific differences in acoustic skull properties, e.g. differences in the skull microstructure or composition that are not resolved at the spatial resolution of clinical CT scanners [36]. The limitations outlined above generally apply and affect the reliability of the simulations, even though the magnitude of the skull modeling uncertainty impact likely depends, e.g., on skull shape, size, species, and especially, how close to the reported and applied attenuation values a particular skull is. Resolving them would likely require reestablishing the mappings based on a CT scanner that is calibrated at higher HU for a specific tube voltage so that they could be transferred to data acquired from other similarly calibrated scanners. Alternatively, dual-energy CT might be used to reliably estimate bone density [23], probably at the expense of increasing the radiation dose.

Impact of the positioning accuracy. Our results confirm the high sensitivity of the simulations to translations and rotations of the transducer relative to the skull. Even changes in the order of 1–2 mm or 2–3° can affect the predictions of both shape and intensity. Here, this was particularly apparent for shifts and direction in the direction along which the cur-

vature or structure of the skull changed the most. For the human skull, the effect might be often less pronounced as the skull composition and curvature does not change as quickly as seen here for the smaller sheep skull. However, the results still point to the need to control the transducer position very accurately in practical applications – despite the skull modeling-related uncertainties, minimizing positioning errors will help converge on the most accurate estimates. For human non-invasive brain stimulation, neuronavigation based on frameless stereotaxy is considered the gold standard for position control. However, its reported accuracy lies within a few millimeter, i.e., in the range that resulted in clear errors in our simulations [38], suggesting the need for improvements. It is also likely that a slight systematic mismatch of the modeled transducer position contributed to the differences between the simulated and measured acoustic beam shape in our case, despite our efforts to precisely control the position. However, systematically searching for the shift and rotation that optimize the simulation and measurement agreement would likely constitute overfitting.

Phased array transducers. This study focuses on a single element transducer. It should be investigated in follow-up work, how the findings translate to phased array transducers, and particularly, how they affect skull phase aberration correction. We suspect that the results will be highly dependent on the chosen phased-array applicator design (e.g., random element positioning vs. structured, varying number of elements) and more importantly, on the focusing strategy.

Measurement uncertainties. While the focus of this study has been on the sensitivity of simulation results to uncertainties of underlying parameters, comparison with experimental measures also requires assessment of the measurement uncertainty. On the sensing side there is the hydrophone sensitivity ($\pm 9\,\%$ according to the calibration document), measurement noise (the low frequency noise was reduced through high-pass filtering, see [19]), and the hydrophone positioning uncertainty. The latter can be separated into uncertainty about the relative positioning of the measurement points, which is negligible in view of the stepper accuracy (accuracy better than 0.02 mm, repeatability <0.003 mm), a systematic positioning bias resulting from scan-plane-tilting or changes in hydrophone positioning before and after skull insertion (estimated to be in the order of 0.5 mm), and finally the peak localization uncertainty in the absence of any obstacle (used to align the measurements and simulations and for normalization). That peak was found by first detecting the maxima in two 0.6 mm resolution planar scans (2 cm apart) near the focus, to verify positioning and detect transducer tilt, and then measuring a perpendicular line through the maxima. In the skull setup, all the planes perpendicular to the beam are measured first and subsequently they are used to define the location of the parallel measurement plane. Due to distortion, the actual peak location might not be measured. The hydrophone sensor has a diameter of 1 mm, which is not negligible compared to the acoustic wavelength in water of approximately 3 mm. It is expected that this impacts the measurement results in two ways, as the exact location of the sensitive element is not known (introducing a positioning uncertainty bias) and as its finite extent can lead to spatial signal averaging. The former only affects absolute localization (not relative positions), as it stays constant while scanning, and is handled as part of the spatial

tolerance in the Gamma metric. The impact of the latter was estimated by comparing the local intensity magnitude to the $1\,\mathrm{mm}^3$ averaged distribution (a maximal difference of 3 % is found in the reference configuration).

On the sonication side, uncertainty factors include amplifier gain (which can vary over time and was minimized by measuring the peak intensity without skull obstacle before each measurement series and normalizing accordingly) and amplifier linearity (minimized by using the same driving voltage throughout all measurement series). In what concerns the reproduction of the measurement setup by the model, there is the relative placement of the transducer, the skull and the hydrophone, as well as uncertainty about the acoustic properties of the holder. The hydrophone insertion in the holder was verified with a ruler (see above), the hydrophone distance to the skull was established with high accuracy by advancing a hydrophone phantom until contact, and the holder shape and location uncertainty are small, thanks to the accuracy of 3D printing and the rigid, fused structure of the hydrophone and skull holders. The pulsed nature of the exposure prevents reflected waves from interfering with the measured pulse, thus avoiding the necessity of accurately capturing holder and wall properties. Reflections from the hydrophone holder are avoided by using an acrylic material with water-like impedance.

In conclusion, the principal uncertainty contributions are expected to originate from the skull heterogeneity modeling (including attenuation) and the skull alignment.

Simulation / measurement agreement. The results (see Figure B.6 in particular) suggest that once the attenuation property assignment has been properly tuned, image-based modeling accounting for skull heterogeneity is capable of predicting transcranial exposure with clinically suitable accuracy (provided that it accurately reproduces the applicator placement), while homogeneous modeling doesn't. The present study suggests that all velocity mapping approaches perform similarly well after scanner-specific calibration. However, it still remains to be investigated, whether and how a suitable patient-specific effective attenuation value can be reliably and universally derived based on scanner-specifically calibrated imaging information.

Study limitations. The presented results mostly reflects measurements performed on a single sample of a sheep skull. Considering the known interspecies and interindividual (e.g. age-related) differences of the acoustic properties of bone [39], it can be expected that the reported results are sample specific and would vary if repeated for other samples. However, we find it unlikely that our conclusions on, e.g. the relevance of specific CT parameters would fundamentally change. In particular, most of our main findings help to reveal general limitations of CT-informed TUS simulations that are independent of the tested sample, but are caused by the procedures used for the CT image acquisition. The generality of our conclusions is supported by the small modeling study performed using human head models. However, that modeling study also indicates that the magnitude of the sensitivity depends on the target location, due to the varying skull structure complexity (evident when comparing the Hand and Leg targets).

Our results indicate that a part of the observed mismatch between simulations and measurements might be due to positioning errors in the measurement. An even more careful

position control might be needed to resolve the remaining mismatch between the spatial distribution of the simulated and measured acoustic waves. Considering the highlighted limitations of the CT data, it is less obvious whether an improved position control would also help to improve the estimation of the magnitude of the acoustic waves.

5. Conclusions

Properly modeling skull heterogeneity is important to accurately predict the acoustic intensity distribution. Interestingly, the structure of the heterogeneity has a much larger impact than the degree of heterogeneity and must be considered to reliably and accurately predict the beam shape. Our study confirms the value of informing TUS simulations by CT-images of the skull heterogeneity. In particular, the image information helps to estimate relative spatial variations of bone density and speed-of-sound within the skull, which improves the accuracy of the simulated spatial distribution of the transmitted wave. Of note, this also works for low-dose CT scans of the head that minimize the exposure of the participants to radiation at the expense of having a lower SNR than standard diagnostic clinical CT scans. On the other hand, reliable estimation of the magnitude of the transmitted wave is still a challenge even when CT information is available. CT scanners are usually not calibrated in the upper HU range that covers bone. Consequently, CT images do not provide reliable quantitative information about the absolute bone density, which in turn reduces the reliability of the estimated speed-of-sound and acoustic attenuation. The uncertainty of these parameters affects mostly the simulated magnitude of the acoustic wave, while its relative spatial distribution seems to be more robustly estimated. In order to ameliorate this problem, some studies chose to use a spatially homogenous attenuation value for the skull that was either empirically adjusted to match the measurements, or – as this is not feasible for human applications – was based on literature values. Indeed, it seems that the best option so far is to base the simulations on linear mappings of the CT information to bone density and speed-of-sound that are adjusted for a scanner-specific upper reference point for compact skull, in combination with using a homogenous skull attenuation. Literature values can be used for the purpose of fixing the reference point properties and attenuation, at the cost of loosing part of the subject-specific information.

Besides their importance in the context of personalized TUS modeling and treatment planning / optimization, the presented results make it evident that particular care is needed when translating a modeling approach from one clinical site to another, as imaging conditions are likely to change.

Our findings also confirm that the transmitted acoustic wave is sensitive to small changes (1–2 mm, 2–3°) of the transducer position relative to the skull. When aiming to use acoustic simulations to inform personalized TUS applications, a precise control of the transducer placement is thus needed that seems to be at the limit of the accuracy provided by currently available neuronavigation systems.

Future progress would benefit from the use of CT scans that are calibrated and quantitative in the upper HU range, which can for example be achieved by using dual-energy scans. This would improve the comparability of simulation results across studies. Trans-

ferability would be further improved when controlling for the image smoothness caused by the reconstruction filter. Importantly, calibrated and standardized CT scans would also ensure that mapping functions between CT information and acoustic bone properties are not scanner-specific, but can be transferred between studies. Our results indicate that this is a key requisite for improving the reliability of CT-based estimates of the acoustic properities of the skull, in particular when aiming to also estimate the attenuation of the skull.

6. Acknowledgements

This study was supported by the Lundbeck Foundation (grants R118-A11308 and R313-2019-622 to AT) and by a PhD stipend of the Technical University of Denmark granted to CP. HRS holds a 5-year professorship in precision medicine at the Faculty of Health Sciences and Medicine, University of Copenhagen which is sponsored by the Lundbeck Foundation (grant R186-2015-2138).

7. Conflicts of interest

Hartwig R. Siebner has received honoraria as speaker from Sanofi Genzyme, Denmark and Novartis, Denmark, as consultant from Sanofi Genzyme, Denmark and as editor-in-chief (NeuroImage Clinical) and senior editor (NeuroImage) from Elsevier Publishers, Amsterdam, The Netherlands. He has received royalties as book editor from Springer Publishers, Stuttgart, Germany and Gyldendal, Copenhagen, Denmark. Niels Kuster is the founder of Schmid & Partner Engineering AG (SPEAG) and ZMT Zurich MedTech AG (ZMT). He is also a minority shareholder of NFT Holding AG that owns shares of SPEAG and ZMT. SPEAG and ZMT provide simulation tools (SEMCAD X and Sim4Life) for assessing exposure of complex anatomies to electromagnetic and acoustic fields, as well as the resulting biological and physiological impact. Esra Neufeld holds a small amount of ZMT shares.

Appendix A. Adjustment of CT noise levels

The level of noise in a CT image does not only depend on the dose and the reconstruction filter, but also on the amount of absorbed X-rays by the scanned object and the surrounding background medium. CT scans of a human head will thus have more noise than a scan of the rather small sheep skull sample used here when keeping the scan settings unchanged. Therefore, we mimic the noise levels of human clinical- or low-dose CT images by adding Gaussian noise to our images taken in a air background to re-create realistic patient scanning conditions. To do that, we considered the noise distribution in a region of interest (ROI) in the brain in a human CT image acquired at low-dose and with H60s reconstruction filter [25]. We first verified that the values in the ROI were normally distributed (Kolmogorov-Smirnov test), and added corresponding Gaussian noise to the CT images of the sheep skull (air background). When two normally distributed random variables X and Y with variances of σ_x^2 and σ_y^2 are summed up, the sum Z has a variance which is the sum of the variances ($\sigma_z^2 = \sigma_x^2 + \sigma_y^2$). In our case, we determined the variance in a ROI in the center of a human low-dose CT image (i.e., not involving skull and assuming that the values for brain and cerebrospinal fluid are close to water) and a ROI in a water glass in the CT data of the sheep skull sample (same CT parameters). We then adjusted the noise level of the sheep skull image by adding Gaussian noise with a variance that corresponded to the difference between the variances of the human and sheep CT scans.

As we had no human CT scan with clinical dose available, we estimated the corresponding noise variance by comparing the variances in ROIs placed in water and in air of sheep CT scans with low versus clinical dose. The variance of the sheep CT scans with clinical dose was then adjusted accordingly by adding Gaussian noise.

Dose	Filter	σ [HU]
High	H60s	17.0
High	H48s	5.2
High	H41s	4.0
Low	H60s	171.0
Clinical	H60s	126.2
Low*	H60s	45.0
Clinical*	H60s	33.9

Table A.1: HU standard deviations (σ) in a water region of interest of 100×100 pixels. Images were acquired at tube voltage 140 kV with varying doses (high, clinical, low) and smoothing filters (H60s, H48s, H41s). The rows marked with an asterisk refer to the original CT data without added noise.

Appendix B. Auxiliary tables and figures

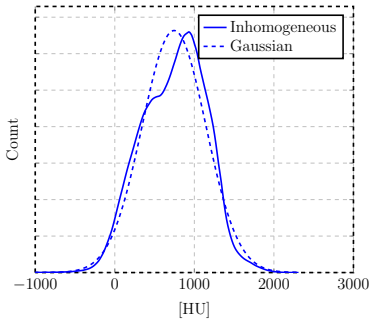

Figure B.1: HU histogram of the skull, as well as fitted Gaussian distribution used to investigate the impact of heterogeneity structure (as opposed to only the heterogeneity level) on transcranial sonication.

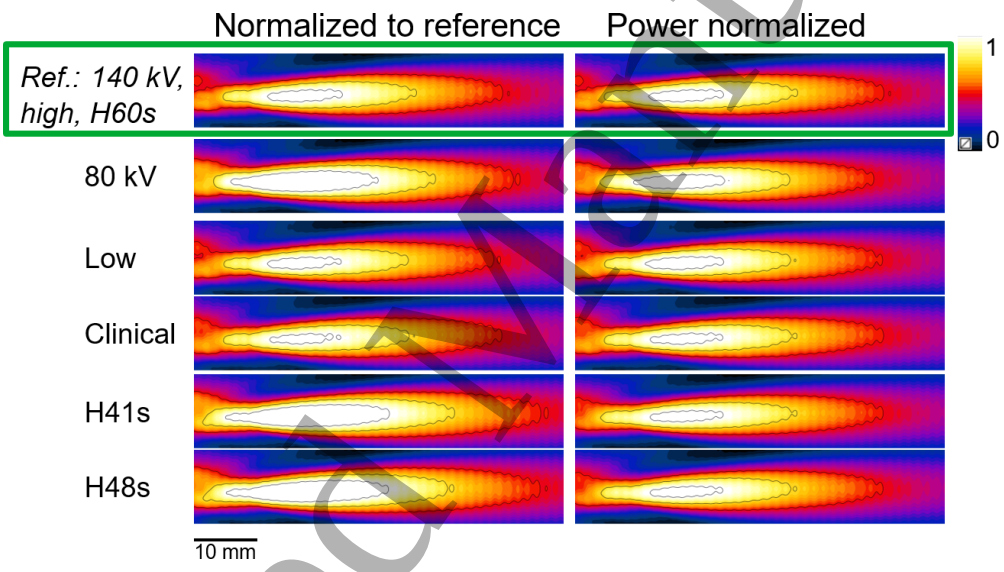

Figure B.2: Assessment of the scan parameter impact on the intensity distribution shape (left: normalization to the reference case's power, right: after normalization to the case-specific deposited power). The reference case, with a tube voltage of 140 kV, high dose and sharp filter (H60s), is at the top highlighted by a green box.

The same scale ranging from zero to the peak value in the measurement is used throughout. Isolines demark 50, 75, and 100 % of that peak value.

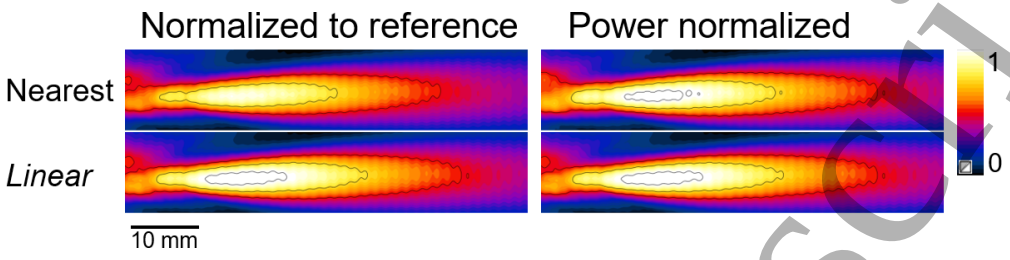

Figure B.3: Same as in Figure B.2, but for the different interpolation schemes for upsampling.

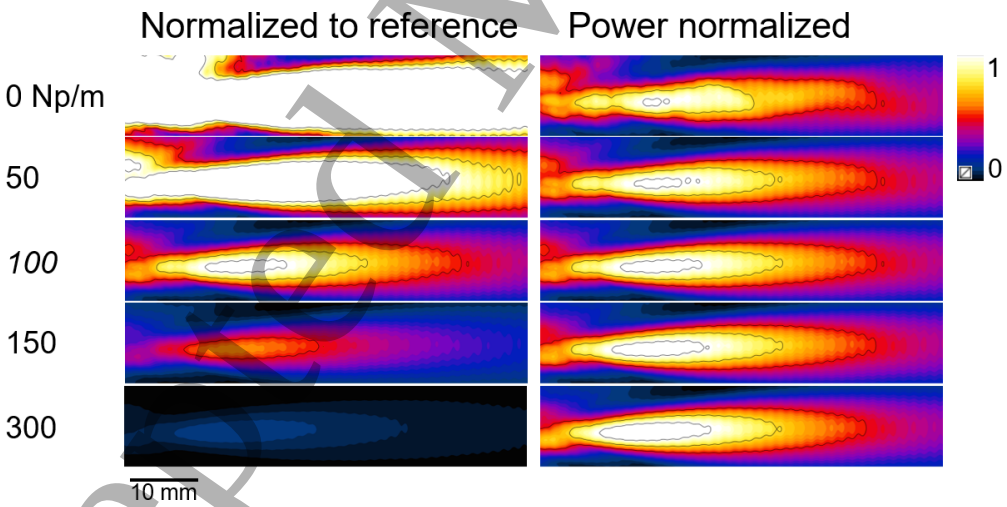

Figure B.4: Same as in Figure B.2, but for different homogeneous skull attenuation values.

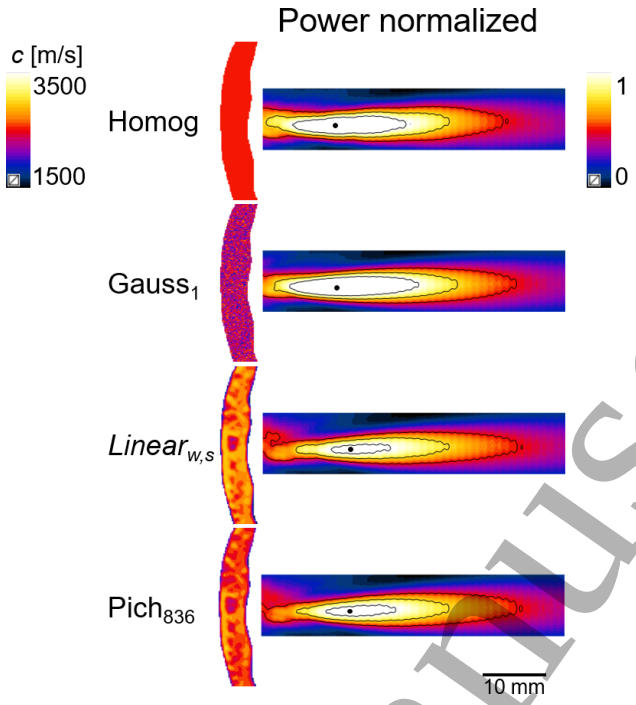

Figure B.5: Impact of skull heterogeneity modeling on the intensity distribution. The color map refers to the skull speed-of-sound distributions (intensity distributions are displayed as in the left columns of Figures B.2–B.4). The location of the peak intensity has been highlighted to illustrate its shift when going from a homogeneous or stochastic heterogeneity model to an image-based heterogeneity model.

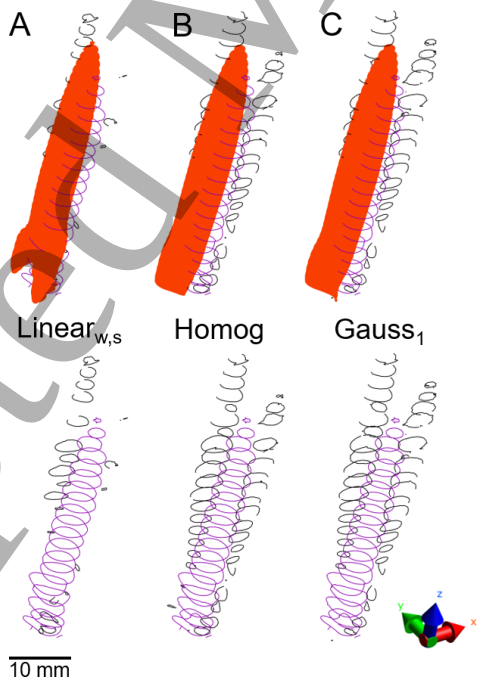

Figure B.6: Impact of skull heterogeneity modeling on the focus shape and γ-distribution. See Figure 6 for an explanation of the different iso-contours and surfaces.

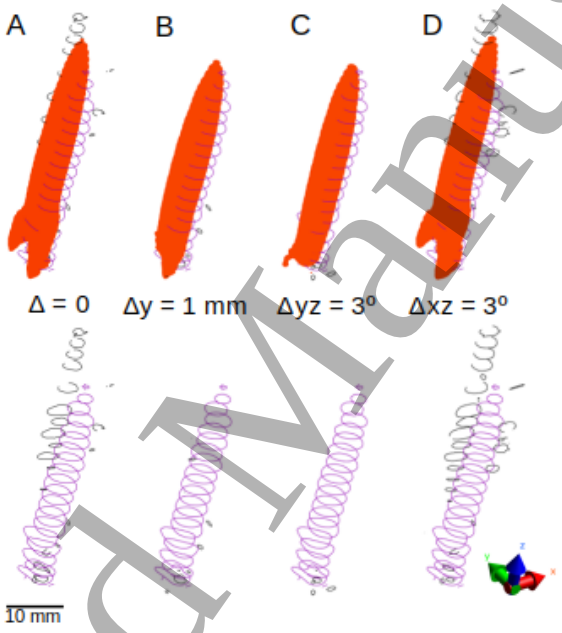

Figure B.7: Same as in Figure B.6, but with varying skull alignment.

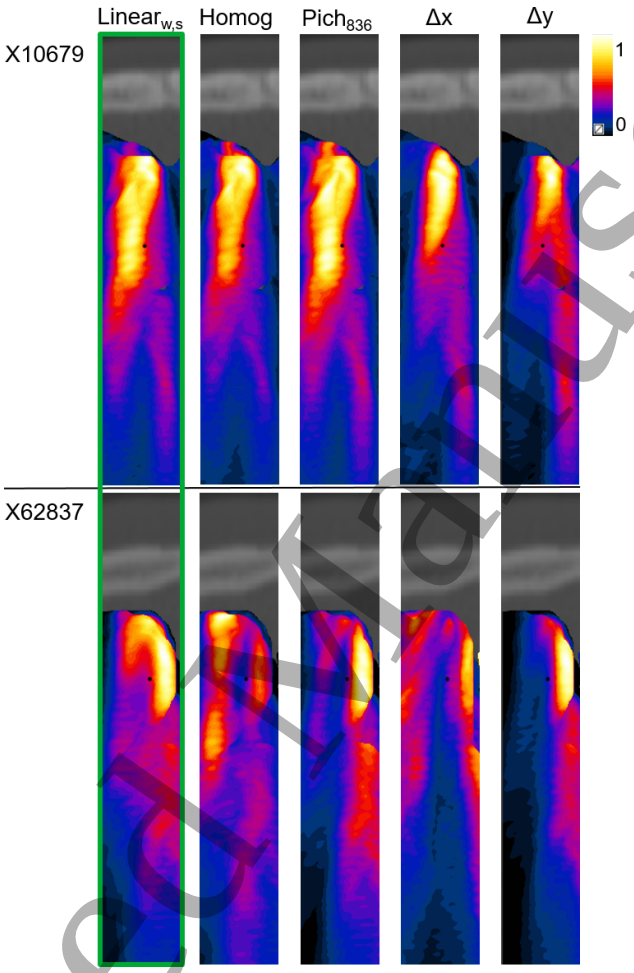

Figure B.8: Maximum intensity projections in brain (white matter and gray matter) normalized by peak intensity of the human TUS simulation results for the left primary motor leg area target and CT-image slice of the skull. The impacts of the skull property mapping approach and transducer shifts are shown for two head models (X10679 and X62837). The associated CT-images are shown and the nearby sagittal suture is apparent for the X10679 model. See Sections 2.4.5 and 3.3.3 for more information. Black dot indicates geometric focus / target location in the brain. Green box indicates configuration used as reference case.

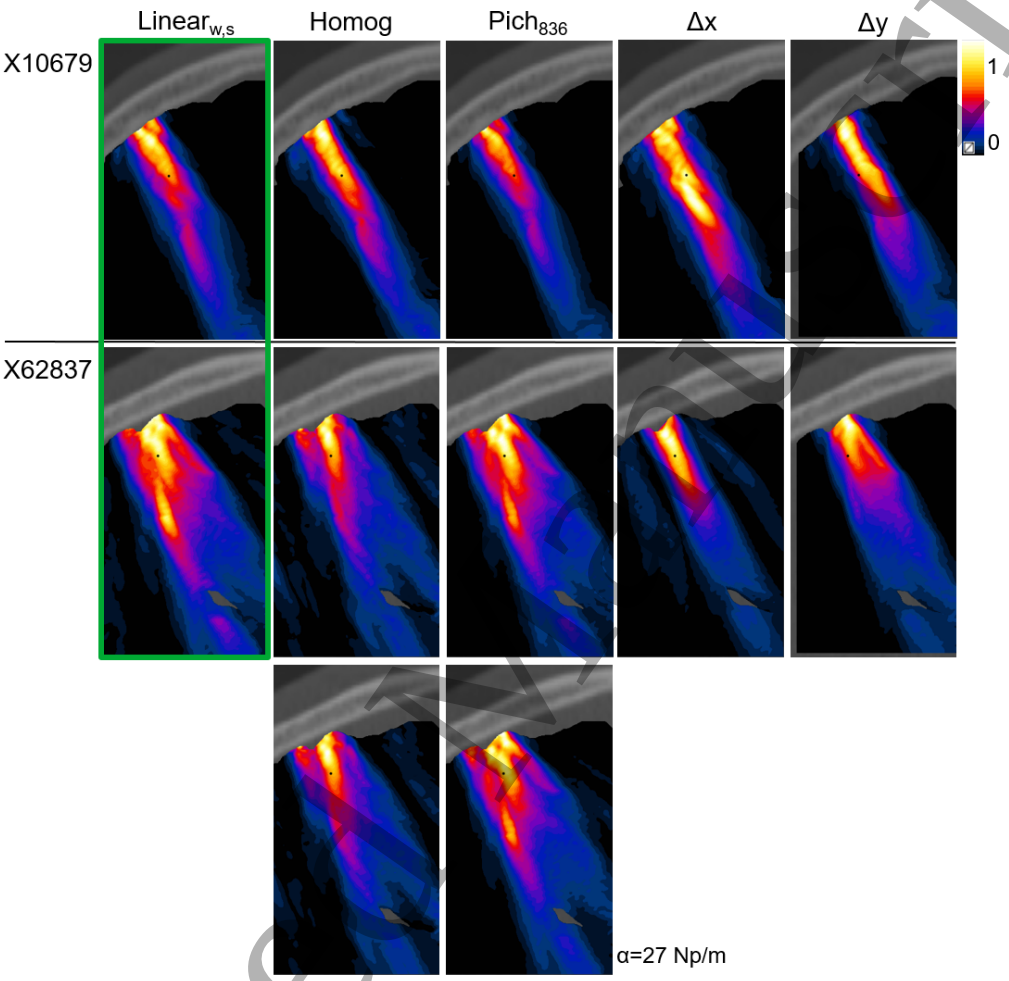

Figure B.9: Maximum intensity projections in brain (white matter and gray matter) normalized by peak intensity of the human TUS simulation results for the left primary motor hand area target and CT-image slice of the skull. The impacts of the skull property mapping approach and transducer shifts are shown for two head models (X10679 and X62837). For the X62837 head model, additional simulations have been performed, in which the same attenuation as for the linear mapping reference simulation was used (third row). See Sections 2.4.5 and 3.3.3 for more information. Black dot indicates geometric focus / target location in the brain. Green box indicates configuration used as reference case.

Factor	Subject	Target	Comparison	ΔI_{peak} [%]	ΔI_{Pnorm} [%]	$\gamma_{\%}$ [%]	$\lvert d \rvert$ [mm]
Mapping	**X10679**	**Leg**	Hom	-69	5	96	1.9
			Pich_{836}	-98	-9	80	7.1
		Hand	Hom	-82	10	29	3.0
			Pich_{836}	-98	38	0	0.2
	X62837	**Leg**	Hom	-63	2	3000	10.4
			Pich_{836}	-99	17	290	4.8
		Hand	Hom	-77	44	2800	7.8
			Pich_{836}	-98	23	0	0.6
			Hom_{27} : Hom	-4	1	0	0.0
			$\text{Pich}_{836,27}$: Pich_{836}	2600	2	1	2.7
			Hom_{27}	-78	44	2700	7.8
			$\text{Pich}_{836,27}$	-35	25	0	2.8
Shifts	**X10679**	**Leg**	Δx	34	31	31000	0.6
			Δy	48	41	19000	3.3
		Hand	Δx	-7	-35	1600	16.3
			Δy	84	5	1500	3.2
	X62837	**Leg**	Δx	-97	-47	49000	3.9
			Δy	48	46	9100	1.6
		Hand	Δx	420	130	32000	4.5
			Δy	490	100	15000	3.3

Table B.2: Impact of skull property mapping and shifts obtained in simulations of human TUS. Metrics are: ΔI_{peak} (peak intensity variation in the brain compared to the reference simulation configuration), ΔI_{Pnorm} (peak intensity variation with reference configuration after both simulations are normalized by their total deposited power), $\gamma_{\%}$ (Gamma metric of power normalized intensity distributions), and $|d|$ (spatial peak location shift with respect to reference configuration). Comparison column indicates simulation configuration; reference simulation is $\text{Linear}_{w,s}$ (linear mapping from HU to speed-of-sound, constant attenuation) unless otherwise specified. Two head models were used (X10679, X62837) and two cortical targets ('Leg', 'Hand') were studied. The following skull property assignment approaches were used: 'Hom' (homogeneous properties, only distinguishing cortical and cancellous) and 'Pich' (nonlinear speed-of-sound and attenuation mappings from [17]). For the X62837 Hand target, the impact of attenuation modeling and skull heterogeneity modeling were separated by considering the following approaches: 'Hom_{27}' and $\text{Pich}_{836,27}$ (same as their counterpart, but with a homogeneous skull attenuation coefficient of 27 Np/m). For shifts Δx and Δy, the skull was modeled as in $\text{Linear}_{w,s}$ and the transducer position was moved by 2 mm in different directions in the transducer plane. See Section 2.4.5 for more details.

References

[1] Alexander Bystritsky, Alex S. Korb, Pamela K. Douglas, Mark S. Cohen, William P. Melega, Amit P. Mulgaonkar, Antonio Desalles, Byoung Kyong Min, and Seung Schik Yoo. A review of low-intensity focused ultrasound pulsation, jul 2011.

[2] Yusuf Tufail, Alexei Matyushov, Nathan Baldwin, Monica L. Tauchmann, Joseph Georges, Anna Yoshihiro, Stephen I Helms Tillery, and William J. Tyler. Transcranial pulsed ultrasound stimulates intact brain circuits. *Neuron*, 66(5):681–94, 2010.

[3] Seung Schik Yoo, Alexander Bystritsky, Jong Hwan Lee, Yongzhi Zhang, Krisztina Fischer, Byoung Kyong Min, Nathan J. McDannold, Alvaro Pascual-Leone, and Ferenc A. Jolesz. Focused ultrasound modulates region-specific brain activity. *NeuroImage*, 56(3):1267–1275, 2011.

[4] Thomas Deffieux, Youliana Younan, Nicolas Wattiez, Mickael Tanter, Pierre Pouget, and Jean François Aubry. Low-intensity focused ultrasound modulates monkey visuomotor behavior. *Current Biology*, 23(23):2430–2433, 2013.

[5] Wonhye Lee, Stephanie D. Lee, Michael Y. Park, Lori Foley, Erin Purcell-Estabrook, Hyungmin Kim, Krisztina Fischer, Lee So Maeng, and Seung Schik Yoo. Image-Guided Focused Ultrasound-Mediated Regional Brain Stimulation in Sheep. *Ultrasound in Medicine and Biology*, 42(2):459–470, 2016.

[6] Dianne Daniels, Shirley Sharabi, David Last, David Guez, Sharona Salomon, Zion Zivli, David Castel, Alex Volovick, Javier Grinfeld, Itay Rachmilevich, Talia Amar, Sigal Liraz-Zaltsman, Narek Sargsyan, Yael Mardor, and Sagi Harnof. Focused Ultrasound-Induced Suppression of Auditory Evoked Potentials in Vivo. *Ultrasound in Medicine and Biology*, 44(5):1022–1030, 2018.

[7] Wonhye Lee, Hyungmin Kim, Yujin Jung, In Uk Song, Yong An Chung, and Seung Schik Yoo. Image-guided transcranial focused ultrasound stimulates human primary somatosensory cortex. *Scientific Reports*, 5:8743, 2015.

[8] Wonhye Lee, Hyun Chul Kim, Yujin Jung, Yong An Chung, In Uk Song, Jong Hwan Lee, and Seung Schik Yoo. Transcranial focused ultrasound stimulation of human primary visual cortex. *Scientific Reports*, 6(1):34026, 2016.

[9] Wonhye Lee, Yong An Chung, Yujin Jung, In Uk Song, and Seung Schik Yoo. Simultaneous acoustic stimulation of human primary and secondary somatosensory cortices using transcranial focused ultrasound. *BMC Neuroscience*, 17(1):68, 2016.

[10] Wynn Legon, Tomokazu F. Sato, Alexander Opitz, Jerel Mueller, Aaron Barbour, Amanda Williams, and William J. Tyler. Transcranial focused ultrasound modulates the activity of primary somatosensory cortex in humans. *Nature Neuroscience*, 17(2):322–329, 2014.

[11] Robert (FDA) Phillips and Gerard (FDA) Harris. Information for Manufacturers Seeking Marketing Clearance of Diagnostic Ultrasound Systems and Transducers. *FDA Guidance*, pages 1–64, 2008.

[12] Arne Voie, Maximilian Dirnbacher, David Fisher, and Thilo Hölscher. Parametric mapping and quantitative analysis of the human calvarium. *Computerized Medical Imaging and Graphics*, 38(8):675–682, 2014.

[13] F J Fry and J E Barger. Acoustical properties of the human skull. *The Journal of the Acoustical Society of America*, 63(5):1576–90, may 1978.

[14] D N White, G R Curry, and R J Stevenson. The acoustic characteristics of the skull. *Ultrasound in Medicine and Biology*, 4(3):225–252, 1978.

[15] J A Evans and M B Tavakoli. Ultrasonic attenuation and velocity in bone. *Physics in Medicine and Biology*, 35(10):1387–1396, oct 1990.

[16] J. F. Aubry, M. Tanter, M. Pernot, J.L. Thomas, and M. Fink. Experimental demonstration of noninvasive transskull adaptive focusing based on prior computed tomography scans. *The Journal of the Acoustical Society of America*, 113(1):84–93, 2003.

[17] Samuel Pichardo, Vivian W. Sin, and Kullervo Hynynen. Multi-frequency characterization of the speed of sound and attenuation coefficient for longitudinal transmission of freshly excised human skulls. *Physics in Medicine and Biology*, 56(1):219–250, 2011.

[18] Christopher W. Connor, Greg T. Clement, and Kullervo Hynynen. A unified model for the speed

of sound in cranial bone based on genetic algorithm optimization. *Physics in Medicine and Biology*, 47(22):3925–3944, 2002.

[19] Cristina Pasquinelli, Hazael Montanaro, Hyunjoo J. Lee, Lars G. Hanson, Hyngkook Hyungguk Kim, Niels Kuster, Hartwig R. Siebner, Esra Neufeld, and Axel Thielscher. Transducer modeling for accurate acoustic simulations of transcranial focused ultrasound stimulation. *Journal of Neural Engineering*, 2020.

[20] Thorsten M Buzug and Dimitris Mihailidis. Computed tomography from photon statistics to modern cone-beam ct. *Medical Physics*, 36:3858, 2009.

[21] James Robertson, Eleanor Martin, Ben Cox, and Bradley E. Treeby. Sensitivity of simulated transcranial ultrasound fields to acoustic medium property maps. *Physics in Medicine and Biology*, 62(7):2559–2580, 2017.

[22] Heinz Morneburg. *Diagnostic Imaging Systems: Diagnostics and Angiography, Computed Tomography, Nuclear Medicine, Magnetic Resonance Imaging, Sonography, Integrated Information Systems*. Publicis MCD-Publisher, 1995.

[23] Taylor D. Webb, Steven A. Leung, Jarrett Rosenberg, Pejman Ghanouni, Jeremy J. Dahl, Norbert J. Pelc, and Kim Butts Pauly. Measurements of the Relationship between CT Hounsfield Units and Acoustic Velocity and How It Changes with Photon Energy and Reconstruction Method. *IEEE Transactions on Ultrasonics, Ferroelectrics, and Frequency Control*, 65(7):1111–1124, jul 2018.

[24] M Tanter, M Fink, L Marsac, J-F Aubry, M Pernot, G Montaldo, F Marquet, M Pernot, J-F Aubry, G Montaldo, L Marsac, M Tanter, and M Fink. Non-invasive transcranial ultrasound therapy based on a 3D CT scan: protocol validation and in vitro results. *Physics in Medicine and Biology*, 54(9):2597–2613, may 2009.

[25] Silvia Farcito, Oula Puonti, Hazael Montanaro, Guilherme B. Saturnino, Jesper D. Nielsen, Camilla G. Madsen, Hartwig R. Siebner, Esra Neufeld, Niels Kuster, Bryn A. Lloyd, and Axel Thielscher. Accurate anatomical head segmentations: a data set for biomedical simulations. In *2019 41st Annual International Conference of the IEEE Engineering in Medicine and Biology Society (EMBC)*, pages 6118–6123. Institute of Electrical and Electronics Engineers (IEEE), oct 2019.

[26] Adamos Kyriakou. *Multi-Physics Computational Modeling of Focused Ultrasound Therapies*. PhD thesis, ETH Zürich, 2015.

[27] Matthew Pelekanos, Gerhard Leinenga, Mostafa Odabaee, Maryam Odabaee, Siamak Saifzadeh, Roland Steck, and Jürgen Götz. Establishing sheep as an experimental species to validate ultrasound-mediated blood-brain barrier opening for potential therapeutic interventions. *Theranostics*, 8(9):2583–2602, 2018.

[28] Thomas Deffieux and Elisa Konofagou. Numerical study of a simple transcranial focused ultrasound system applied to blood-brain barrier opening. *IEEE Transactions on Ultrasonics, Ferroelectrics, and Frequency Control*, 57(12):2637–2653, 2010.

[29] Silvia Farcito, Oula Puonti, Hazael Montanaro, Guilherme B Saturnino, Jesper D Nielsen, Camilla G Madsen, Hartwig R Siebner, Esra Neufeld, Niels Kuster, Bryn A Lloyd, et al. Accurate anatomical head segmentations: a data set for biomedical simulations. In *2019 41st Annual International Conference of the IEEE Engineering in Medicine and Biology Society (EMBC)*, pages 6118–6123. IEEE, 2019.

[30] PA Hasgall, E Neufeld, MC Gosselin, A Klingenböck, and N Kuster. It'is database for thermal and electromagnetic parameters of biological tissues. *Version 3.0*, 2015.

[31] Daniel A Low. Gamma dose distribution evaluation tool. In *Journal of Physics: Conference Series*, volume 250, pages 349–359. IOP Publishing, nov 2010.

[32] Esra Neufeld, Adamos Kyriacou, Wolfgang Kainz, and Niels Kuster. Approach to Validate Simulation-Based Distribution Predictions Combining the Gamma-Method and Uncertainty Assessment: Application to Focused Ultrasound. *Journal of Verification, Validation and Uncertainty Quantification*, 1(3):031006, 2016.

[33] P. J. White, G. T. Clement, and K. Hynynen. Transcranial longitudinal and shear sound speeds in animal models. *The Journal of the Acoustical Society of America*, 119(5):3319–3319, may 2013.

[34] Kyungho Yoon, Wonhye Lee, Phillip Croce, Amanda Cammalleri, and Seung Schik Yoo. Multi-resolution simulation of focused ultrasound propagation through ovine skull from a single-element

transducer. *Physics in Medicine and Biology*, 63(10):0–18, 2018.

[35] Rokuro Hatakeyama, Masazumi Yoshizawa, and Tadashi Moriya. Method for the measurement of acoustic impedance and speed of sound in a small region of bone using a fused quartz rod as a transmission line. *Japanese Journal of Applied Physics, Part 1: Regular Papers and Short Notes and Review Papers*, 39(11):6449–6454, 2000.

[36] James Robertson, Jillian Urban, Joel Stitzel, and Bradley E. Treeby. The effects of image homogenisation on simulated transcranial ultrasound propagation. *Physics in Medicine and Biology*, 63(14), 2018.

[37] Can Barlş Top, P. Jason White, and Nathan J. McDannold. Nonthermal ablation of deep brain targets: A simulation study on a large animal model. *Medical Physics*, 43(2):870–882, jan 2016.

[38] Carlos Schönfeldt-Lecuona, Axel Thielscher, Roland W. Freudenmann, Martina Kron, Manfred Spitzer, and Uwe Herwig. Accuracy of stereotaxic positioning of transcranial magnetic stimulation. *Brain Topography*, 17(4):253–259, jul 2005.

[39] S. A. Goss, R. L. Johnston, and F. Dunn. Comprehensive compilation of empirical ultrasonic properties of mammalian tissues. *Journal of the Acoustical Society of America*, 64(2):423–457, 1978.